

INTERSTELLAR GAS AND X-RAYS TOWARD THE YOUNG SUPERNOVA REMNANT RCW 86; PURSUIT OF THE ORIGIN OF THE THERMAL AND NON-THERMAL X-RAY

H. SANO^{1, 2}, E. M. REYNOSO³, I. MITSUISHI², K. NAKAMURA², N. FURUKAWA², K. MRUGANKA⁴, T. FUKUDA², S. YOSHIIKE², A. NISHIMURA², A. OHAMA², K. TORII⁵, T. KUWAHARA², T. OKUDA⁶, H. YAMAMOTO², K. TACHIARA², Y. FUKUI^{1, 2}

¹Institute for Advanced Research, Nagoya University, Furo-cho, Chikusa-ku, Nagoya 464-8601, Japan; sano@a.phys.nagoya-u.ac.jp

²Department of Physics, Nagoya University, Furo-cho, Chikusa-ku, Nagoya 464-8601, Japan

³Instituto de Astronomía y Física del Espacio (IAFE, CONICET-UBA), Av. Int. Gúraldes 2620, Pabellón IAFE, Ciudad Universitaria, Ciudad Autónoma de Buenos Aires, Argentina

⁴Department of Electrical and Computer Engineering, University of California, San Diego, La Jolla, CA 92093-0407, U.S.A.

⁵Nobeyama Radio Observatory, Minamimaki-mura, Minamisaku-gun, Nagano 384-1305, Japan and

⁶National Astronomical Observatory of Japan, Mitaka, Tokyo 181-8588, Japan

accepted version (26th April 2017)

ABSTRACT

We have analyzed the atomic and molecular gas using the 21 cm H I and 2.6/1.3 mm CO emissions toward the young supernova remnant (SNR) RCW 86 in order to identify the interstellar medium with which the shock waves of the SNR interact. We have found an H I intensity depression in the velocity range between -46 and -28 km s⁻¹ toward the SNR, suggesting a cavity in the interstellar medium. The H I cavity coincides with the thermal and non-thermal emitting X-ray shell. The thermal X-rays are coincident with the edge of the H I distribution, which indicates a strong density gradient, while the non-thermal X-rays are found toward the less dense, inner part of the H I cavity. The most significant non-thermal X-rays are seen toward the southwestern part of the shell where the H I gas traces the dense and cold component. We also identified CO clouds which are likely interacting with the SNR shock waves in the same velocity range as the H I, although the CO clouds are distributed only in a limited part of the SNR shell. The most massive cloud is located in the southeastern part of the shell, showing detailed correspondence with the thermal X-rays. These CO clouds show an enhanced CO $J = 2-1/1-0$ intensity ratio, suggesting heating/compression by the shock front. We interpret that the shock-cloud interaction enhances non-thermal X-rays in the southwest and the thermal X-rays are emitted by the shock-heated gas of density $10-100$ cm⁻³. Moreover, we can clearly see an H I envelope around the CO cloud, suggesting that the progenitor had a weaker wind than the massive progenitor of the core-collapse SNR RX J1713.7-3949. It seems likely that the progenitor of RCW 86 was a system consisting of a white dwarf and a low-mass star with low-velocity accretion winds.

Subject headings: cosmic rays – ISM: clouds – ISM: individual objects (RCW 86) – ISM: supernova remnants – X-rays: ISM

1. INTRODUCTION

RCW 86 (also known as MSH 14-63 or G315.4-2.3) is one of the supernova remnants (SNRs) that has been detected in the whole electromagnetic spectrum, from the radio continuum, optical, and infrared domains to the energetic X-rays and GeV/TeV γ -rays (e.g., Kesteven & Caswell 1987; Smith 1997; Williams et al. 2011; Broersen et al. 2014; Ajello et al. 2016; H. E. S. S. Collaboration et al. 2016). Of particular interest are the bright TeV γ -rays and non-thermal X-rays, which are tightly related with the production of cosmic-rays (CRs) via the diffusive shock acceleration (DSA) mechanism in SNRs (Bell 1978; Blandford & Ostriker 1978). RCW 86 is therefore suitable for studying the origin of Galactic CRs in an energy range $E < 3 \times 10^{15}$ eV and their relationship with the surrounding interstellar medium (ISM) by using multi-wavelength datasets.

RCW 86 is a relatively young SNR, first recorded in AD 185 in the Chinese historical book *Houhanshu* (Clark & Stephenson 1975; Zhao et al. 2006). The SNR is located slightly away from the Galactic plane (l, b) $\sim (315^\circ.4, -2^\circ.3)$, at only ~ 2.5 kpc from us (e.g., Westerlund 1969; Rosado et al. 1996; Helder et al. 2013,

by association with the edge of the molecular supershell GS 314.8-0.1-34 discovered by Matsunaga et al. 2001). The shell-like morphology of RCW 86 was first discovered in radio continuum observations (Mills et al. 1961; Hill 1967). After half a century, such morphology has been confirmed at all wavelengths, including γ -rays. The observed diameter is approximately 40 arcmin, corresponding to a diameter of ~ 30 pc at 2.5 kpc. The progenitor system of RCW 86 (Type Ia or core-collapse (CC)) remains contentious. The CC hypothesis is supported by the presence of several B-type stars in the neighbourhood of RCW 86 (Westerlund 1969). However, recent optical and X-ray studies reporting Fe-rich ejecta and Balmer filaments encircling the shell suggest a Type Ia explosion (e.g. Smith 1997; Yamaguchi et al. 2011; Williams et al. 2011; Broersen et al. 2014). Besides, RCW 86 lacks a central compact object such as a neutron star or region of O-rich ejecta. Therefore, it is unlikely that RCW 86 is a CC SNR. According to numerical simulations, the progenitor system is also consistent with an off-centered Type Ia explosion (e.g., Williams et al. 2011).

RCW 86 has received much attention since the discovery of TeV γ -ray emission with the high-energy stereoscopic system (H.E.S.S.) by Aharonian et al. (2009). The

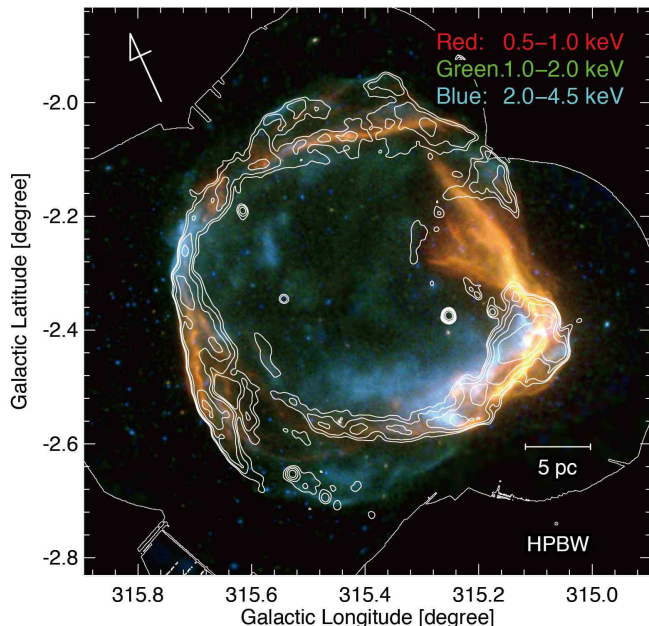


FIG. 1.— Three-color image of the SNR RCW 86 observed by *XMM-Newton*. The red, green, and blue colors represent the energy bands, 0.5–1.0, 1.0–2.0, and 2.0–4.5 keV, respectively. The white solid line indicates the region observed with the MOS and PN detectors. Contours represent the MOST radio continuum at a frequency of 843 MHz (Whiteoak & Green 1996). The contour levels are 5, 10, 20, 40, 80, and 160 mJy beam⁻¹.

TeV γ -ray flux of RCW 86 is ten times lower than that of the Crab nebula, but the origin of which is not yet settled. Subsequently, Lemoine-Goumard et al. (2012) and Yuan et al. (2014) obtained GeV γ -ray images and spectra with the *Fermi* Large Area Telescope (LAT). By using a broad-band spectral energy distribution (SED) fitting, they also discussed whether the γ -rays are hadronic or leptonic in origin. They concluded that the leptonic origin was more reasonable, but the low photon statistics did not rule out a hadronic origin. Recently, H. E. S. S. Collaboration et al. (2016) analyzed the new H.E.S.S. dataset and revealed the shell-like morphology in TeV γ -rays, the origin of which is not yet discerned. Most recently, Ajello et al. (2016) obtained new GeV γ -ray images and spectra from a 6.5-year dataset of *Fermi* LAT. They concluded that the broad-band SED favors the leptonic origin under the two-zone model. If the process is hadronic, the γ -rays should spatially correspond to the interstellar gas (e.g., Aharonian et al. 2008; Fukui et al. 2012; Yoshiike et al. 2013; Fukuda et al. 2014). Therefore, a detailed spatial comparison between the interstellar gas and γ -rays is highly desirable in order to establish origin of the high energy emission.

Studies of the ISM in SNR environments have improved our understanding of SNR evolution, shock heating/ionization, acceleration of CRs, and high-energy radiation (e.g., Fukui et al. 2012; Inoue et al. 2012; Yoshiike et al. 2013; Sano et al. 2013). In RCW 86, however, deep studies of the ISM have not been reported. Williams et al. (2011) revealed the interstellar dust distribution of RCW 86 using the *Spitzer Space Telescope* and the *Wide-Field Infrared Survey*

Explorer (WISE). They noted the distribution of thin dust filaments in the east region, which appear to trace the SNR shockwaves. In contrast, neutral atomic gas (HI) forms a cavity-like structure at radial velocities of approximately -34 km s⁻¹ (Ajello et al. 2016; Duvidovich et al. 2016), although the detailed velocity structure and its relationship with the SNR shockwaves have not been presented. In particular, observations of molecular clouds traced by carbon monoxide (CO) emission have not been attempted to date. In proper-motion measurements, the shock velocity was found to differ from region to region perhaps owing to the inhomogeneous interstellar environment and/or different stages of interaction with the surroundings (e.g., Vink et al. 1997; Helder et al. 2013). The highest shock velocity ($\sim 3,000$ km s⁻¹) occurs in the northeast region, which mainly comprises non-thermal X-rays (Helder et al. 2013; Yamaguchi et al. 2016). Conversely, the lowest shock velocities (500–900 km s⁻¹) are observed in the southwest and northwest regions, which strongly emit thermal X-rays (Long & Blair 1990; Ghavamian et al. 2001). Moreover, according to Rho et al. (2002) and Yamaguchi et al. (2011), interactions between the dense clouds and SNR shockwaves manifest as reverse or secondary shocks in some parts of the shell.

In the present study, we aim to identify the interstellar molecular/atomic gas distribution associated with RCW 86 and to compare it with the thermal/non-thermal X-rays, radio continuum, and H α datasets. We seek for the physical connection between the surrounding gas components, and pursuit the origin of the thermal/non-thermal X-rays, shock properties, and the progenitor system of the SNR. In a subsequent paper, we will compare the shock-interacting gas and TeV γ -rays (Sano et al. 2017, in preparation). Section 2 presents the observations and data reduction of NANTEN2 CO, ATCA & Parkes HI, *XMM-Newton* X-rays, and the datasets at the other wavelengths. Section 3 comprises four subsections. Subsection 3.1 overviews the CO, HI, and X-ray distributions; subsections 3.2 and 3.3 present a detailed analysis of the distributions and physical conditions of CO and HI respectively; and subsection 3.4 presents a detailed comparison between these and the X-ray distributions. Discussion and conclusions are presented in Sections 4 and 5, respectively.

2. OBSERVATIONS & DATA REDUCTIONS

2.1. CO

We performed ¹²CO($J = 1-0$, $2-1$) observations with NANTEN2 4 m millimeter/sub-millimeter telescope at Pampa la Bola in northern Chile (4,865 m above sea level). Observations of the ¹²CO($J = 1-0$) emission line at 115 GHz were conducted from December 2012 to January 2013. The front end was a 4-K cooled superconductor-insulator-superconductor (SIS) mixer receiver. The double-sideband (DSB) system temperature was ~ 110 K toward the zenith including the atmosphere. The back end was a digital Fourier transform spectrometer (DFS) with 16,384 channels of 1 GHz bandwidth, corresponding to a velocity coverage of $\sim 2,600$ km s⁻¹. Frequency and velocity resolutions were 61 kHz and ~ 0.16 km s⁻¹ ch⁻¹, respectively. We used

TABLE 1
BASIC INFORMATION OF *XMM-Newton* OBSERVATIONS

Observation ID	α_{J2000} (degree)	δ_{J2000} (degree)	Start Date (yyyy-mm-dd hh:mm:ss)	End Date (yyyy-mm-dd hh:mm:ss)	Exposure		
					MOS1 (ks)	MOS2 (ks)	PN (ks)
0110010701	220.73	-62.63	2000-08-16 04:04:38	2000-08-16 10:43:07	17	16	15
0110011301	221.31	-62.41	2000-08-16 12:03:46	2000-08-16 17:37:28	11	11	5
0110011401	220.51	-62.22	2000-08-16 20:18:03	2000-08-17 01:36:33	9	10	6
0110010501	220.14	-62.60	2001-08-17 11:47:26	2001-08-17 16:25:47	9	7	3
0110012501	220.24	-62.72	2003-03-04 09:46:14	2003-03-04 13:11:34	8	9	6
0208000101	221.26	-62.34	2004-01-26 22:30:59	2004-01-27 15:12:51	46	47	44
0504810101	221.57	-62.30	2007-07-28 07:45:25	2007-07-29 16:12:53	95	98	76
0504810601	221.57	-62.30	2007-07-30 15:45:31	2007-07-31 01:52:21	18	19	16
0504810201	221.40	-62.47	2007-08-13 17:42:42	2007-08-14 14:37:56	50	55	37
0504810401	220.15	-62.60	2007-08-23 03:17:26	2007-08-23 23:33:12	62	62	50
0504810301	220.50	-62.22	2007-08-25 02:49:31	2007-08-25 23:34:05	61	62	44
0724940101	221.22	-62.68	2014-01-27 18:48:07	2014-01-29 00:03:07	96	95	77

NOTE. — All exposure times correspond to the flare-filtered exposure.

the on-the-fly (OTF) mode with Nyquist sampling, and the observed area was one square degree. After convolving the datacube with a Gaussian kernel of ~ 90 arcsec (FWHM), the typical noise level was 0.42 K ch^{-1} . The final beam size was ~ 180 arcsec (FWHM). The pointing accuracy was checked every 3 hours. An offset better than ~ 25 arcsec was achieved. The absolute intensity was calibrated by observing IRAS 16293-2422 [$\alpha(J2000) = 16^{\text{h}}32^{\text{m}}23.3^{\text{s}}$, $\delta(J2000) = -24^{\circ}28'39''.2$] (Ridge et al. 2006).

Observations of the $^{12}\text{CO}(J = 2-1)$ emission line at 230 GHz were conducted in November 2008. The front end was a 4-K cooled SIS mixer. The system temperature in DSB was ~ 120 K toward the zenith including the atmosphere. We used an acousto-optical spectrometer with 2,048 channels of 250 MHz bandwidth corresponding to a velocity coverage of $\sim 385 \text{ km s}^{-1}$. The frequency and velocity resolutions were 250 kHz and $\sim 0.38 \text{ km s}^{-1} \text{ ch}^{-1}$, respectively. We used the OTF mode with Nyquist sampling, and the observed area was ~ 0.88 square degrees. After convolving the datacube with a Gaussian kernel of ~ 45 arcsec (FWHM), the typical one sigma noise fluctuations were less than 0.3 K ch^{-1} . The final smoothed beam size was ~ 90 arcsec (FWHM). The pointing error was less than 15 arcsec, and the intensity calibration was applied by observing Oph EW4 [$\alpha(J2000) = 16^{\text{h}}26^{\text{m}}21.92^{\text{s}}$, $\delta(J2000) = -24^{\circ}25'40''.4(J2000)$] (Kulesa et al. 2005).

2.2. HI

We performed HI observations at 1420 MHz using the Australia Telescope Compact Array (ATCA), which consists of six 22-m dishes located at Narrabri, Australia. Observations were conducted during 13 hours on March 24-25, 2002, with the ATCA in the EW 367 configuration (baselines from 46 to 367 m, or from 0.3 to 1.75 k λ , excluding the 6th antenna). We employed the mosaicking technique, with 45 pointings covering an area of ~ 4 square degrees. The absolute flux density scale was determined by observing PKS B1934-638, which was used as the primary amplitude and bandpass calibrator. We also periodically observed PKS 1352-63 for gain and phase calibration. Data reduction was performed by

using the MIRIAD software package (Sault et al. 1995). The images were retrieved using a superuniform weighting and keeping only visibilities shorter than 1.1 k λ . To include extended emission, we combined the ATCA data-set with single-dish observations performed with the Parkes 64 m telescope. The final beam size is 160 arcsec \times 152 arcsec with a position angle of -3° . Typical noise level is $1.0 \text{ K at } 0.82 \text{ km s}^{-1}$ velocity resolution. The data are identical to those published by Ajello et al. (2016).

2.3. X-rays

Twelve *XMM-Newton* pointed observation data are available for RCW 86 as summarized in Table 1. We analyzed both the EPIC-pn and EPIC-MOS datasets by using the HEASoft version 6.18 and the *XMM-Newton* Science Analysis System (SAS) version 15.0. We reprocessed the observation data files following standard procedures provided by the *XMM-Newton* extended source analysis software (ESAS, Kuntz & Snowden 2008). In order to create instrumental background-subtracted, exposure-corrected, adaptively-smoothed images, we prepared exposure maps and quiescent particle background (QPB) images for each observation by using the mos-/pn-filter and mos-/pn-back tasks. Then, we combined the images after subtracting the QPB, and the combined images were divided by the merged exposure maps. An adaptive smoothing process was also applied to emphasize diffuse components with the pixel size of $4''$. Finally, we obtained QPB-subtracted, exposure-corrected, adaptively-smoothed images in the energy bands of 0.5-1.0 (soft) / 1.0-2.0 (middle) / 2.0-4.5 (hard) / 0.5-4.5 (broad) keV. In this analysis, high background periods are removed and the net exposure time is shown in Table 1. Figure 1 shows an X-ray tricolor image of RCW 86. The red, green, and blue regions emit at 0.5-1.0 keV (soft band), 1.0-2.0 keV (medium band), and 2.0-4.5 keV (hard band), respectively. The soft and hard bands are dominated by continuum radiation from thermal plasma and synchrotron X-rays produced by the TeV CR electrons, respectively (Rho et al. 2002; Ajello et al. 2016).

In the present paper, we shall hereafter refer to the

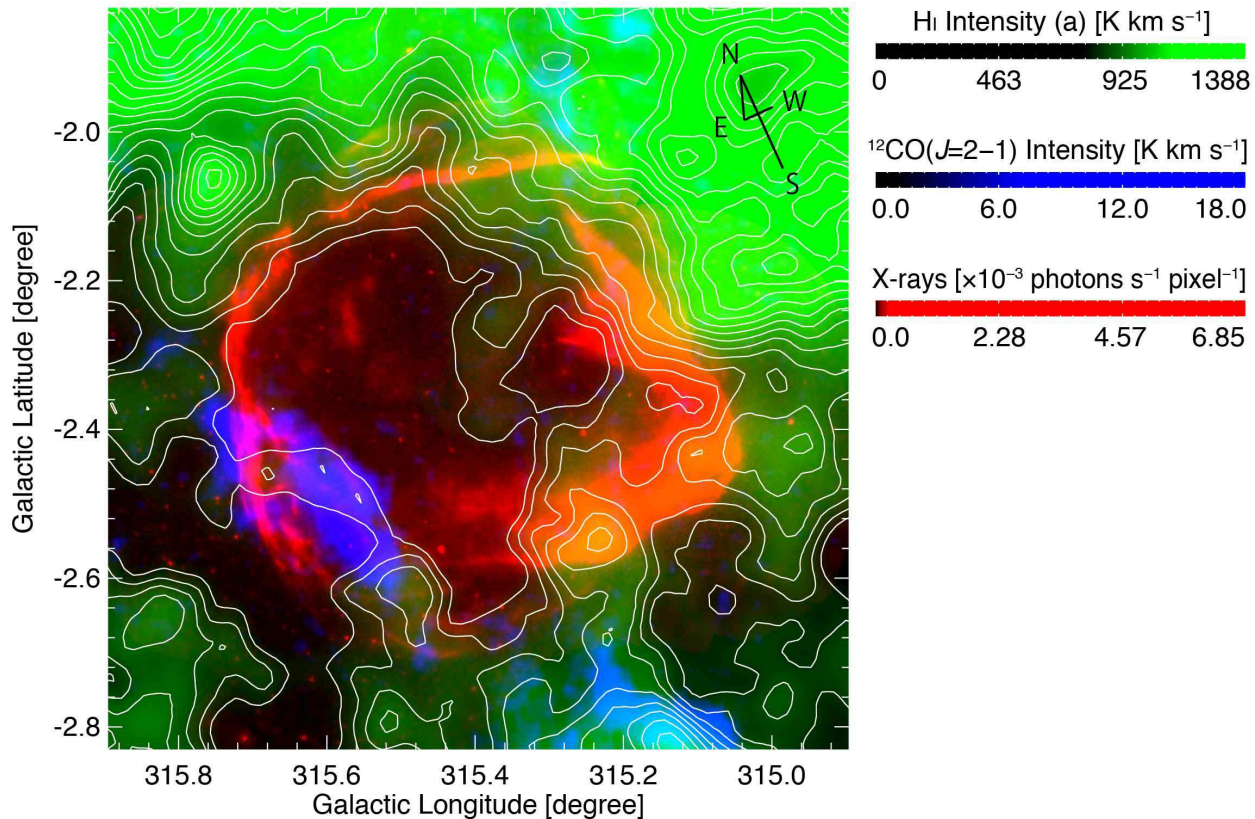


FIG. 2.— Three-color images of the SNR RCW 86 and its surroundings. The red, blue, and green colors represent the *XMM-Newton* broad-band X-rays (0.5–4.5 keV), NANTEN2 $^{12}\text{CO}(J = 2-1)$, and the ATCA & Parkes HI, respectively. The velocity range of CO and HI is from -46.0 to -28.0 km s^{-1} . The contours indicate the HI integrated intensity. The lowest contour level and the contour interval are 806.4 K km s^{-1} ($\sim 240\sigma$) and 33.6 K km s^{-1} ($\sim 10\sigma$), respectively.

emission seen in the image in the soft band as “thermal X-rays” and that of the hard band as “non-thermal X-rays” because each energy band is dominated by the continuum radiation from thermal plasma and non-thermal synchrotron X-rays, respectively (e.g., Rho et al. 2002; Ajello et al. 2016). Moreover, thermal X-rays are dominated by the ISM plasma components, whose distribution is significantly different from the ejecta component except for the SW region (Yamaguchi et al. 2011).

2.4. Astronomical Data at the Other Wavelengths

$\text{H}\alpha$ and radio continuum data are used to derive the spatial distribution of the ionized gas and low-energy CR electrons. We used the $\text{H}\alpha$ and 843 MHz radio continuum data that appear in the Southern H-Alpha Sky Survey Atlas (SHASSA; Gaustad et al. 2001) and the Molonglo Observatory Synthesis Telescope (MOST) Supernova Remnant Catalogue (MSC; Whiteoak & Green 1996), in addition to the CO/HI and X-ray data. The angular resolutions of $\text{H}\alpha$ and radio continuum are 48 arcsec and 43 arcsec, respectively.

3. RESULTS

3.1. Overview of CO, HI, and X-ray Distributions

To determine the velocity range of the atomic and molecular gas associated with the SNR RCW 86, we carried out the following steps:

1. Searching by visual inspection for a good spatial correspondence between the ISM and X-ray intensities in the velocity channel distribution of CO/HI overlaid upon the X-ray contours (see Appendix and Figure A.1);
2. Investigating the physical conditions of associated molecular clouds using the $^{12}\text{CO } J = 2-1/1-0$ intensity ratio maps (see Section 3.2);
3. Exploring possible evidences of expanding motions of HI and CO due to the SNR shockwaves and/or stellar winds from the progenitor of RCW 86 (see Section 3.3).

This analysis led us to conclude that the gas associated with RCW 86 is most likely found at a velocity range from -46 to -28 km s^{-1} . The ATCA & Parkes HI and NANTEN2 $^{12}\text{CO}(J = 2-1)$ emissions integrated in this velocity range are displayed in green and blue, respectively, in Figure 2, together with the *XMM-Newton* X-ray image (red: 0.5–4.5 keV) of RCW 86.

Towards the north, there is an HI intensity gradient increasing from east to west, and the most prominent features, with intensities above $1,000$ K km s^{-1} , lie in the northwest region. The overall distribution of the HI clouds tend to encircle the X-ray shell-like structure. We also find that the diffuse HI gas, with an intensity of ~ 700 K km s^{-1} , fills the interior of the SNR shell. To

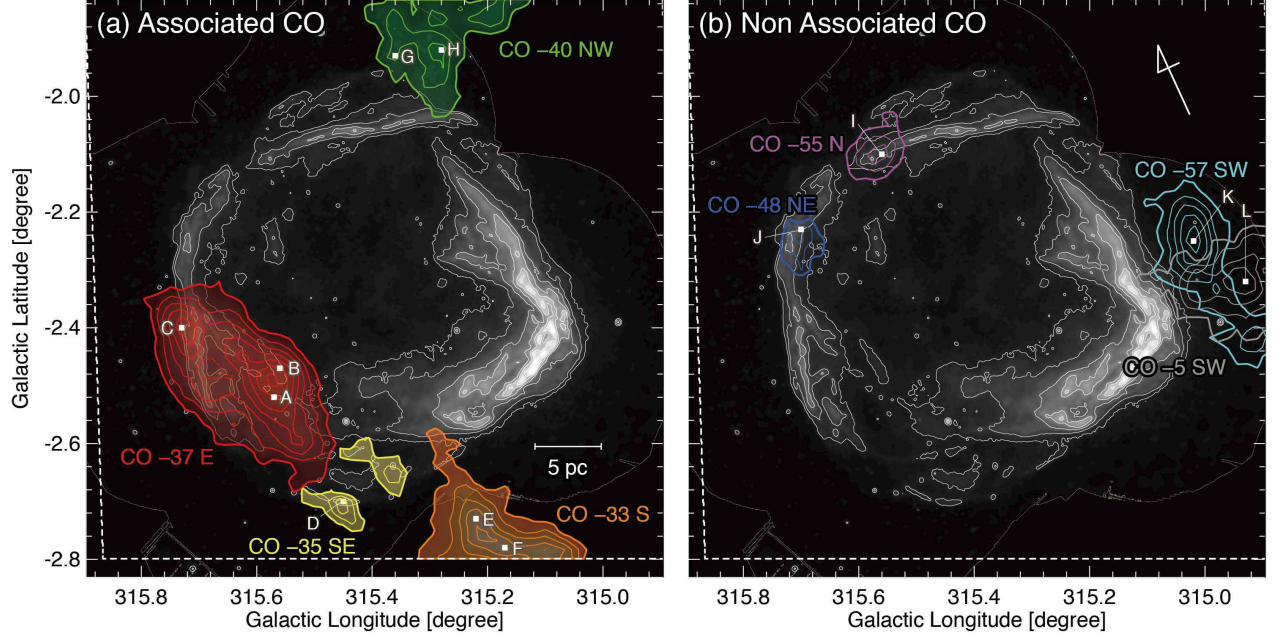


FIG. 3.— Maps of the (a) associated and (b) non-associated $^{12}\text{CO}(J=1-0)$ clouds shown by colored contours. White contours indicate the X-ray intensity in the energy band from 0.5 to 4.5 keV. The contour levels are 6.00×10^{-5} , 1.42×10^{-4} , 3.87×10^{-4} , 7.95×10^{-4} , 1.37×10^{-3} , 2.10×10^{-3} , and 3.00×10^{-3} photons $\text{s}^{-1} \text{pixel}^{-1}$. The integration velocity ranges are as follows: -39.0 to -34.4 km s^{-1} for CO -37 E (contours: lowest $\sim 1.4 \text{ K km s}^{-1}$, intervals $\sim 2.6 \text{ K km s}^{-1}$), -34.0 to -35.6 km s^{-1} for CO -35 SE (contours: lowest $\sim 0.9 \text{ K km s}^{-1}$, intervals $\sim 0.6 \text{ K km s}^{-1}$), -35.9 to -29.3 km s^{-1} for CO -33 S (contours: lowest $\sim 1.8 \text{ K km s}^{-1}$, intervals $\sim 2.5 \text{ K km s}^{-1}$), -44.3 to -35.2 km s^{-1} for CO -40 NW (contours: lowest and intervals $\sim 2.1 \text{ K km s}^{-1}$), -56.0 to -54.4 km s^{-1} for CO -55 N (contours: lowest $\sim 0.9 \text{ K km s}^{-1}$, intervals $\sim 1.6 \text{ K km s}^{-1}$), -48.6 to -46.5 km s^{-1} for CO -48 NE (contours: lowest $\sim 0.7 \text{ K km s}^{-1}$, intervals $\sim 1.1 \text{ K km s}^{-1}$), -57.8 to -55.7 km s^{-1} for CO -57 SW (contours: lowest $\sim 1.1 \text{ K km s}^{-1}$, intervals $\sim 1.8 \text{ K km s}^{-1}$), and -4.9 to -4.1 km s^{-1} for CO -5 SW (contours: lowest and intervals $\sim 0.8 \text{ K km s}^{-1}$). The positions of CO peaks detected at different radial velocities (see Table 2) are identified by letters (A–L).

the east, a large CO cloud with diffuse HI emission is located toward the X-ray filaments. The high angular resolution of CO allowed us to see that the X-ray emission of the filament located around $(l, b) \sim (315^\circ 7', -2^\circ 5')$ is higher where the emission of the CO cloud is lower. The CO clouds are located not only at the east but also at the south and the northwest. Four additional CO clouds are visible toward the SNR: CO -57 SW, CO -55 N, CO -48 NE, and CO -5 SW (Figure 3b). These are probably not interacting with the SNR because their radial velocities do not coincide with those of the associated CO clouds. Hereafter, we shall focus on the velocity range from -46 to -28 km s^{-1} which contains the associated CO clouds.

Figure 3a shows the distribution of the molecular clouds associated with the SNR. These clouds are named CO -40 NW, CO -37 E, CO -35 SE, and CO -33 S, respectively, and their peak radial velocities are derived from a single Gaussian fitting. The basic physical properties of the CO clouds are listed in Table 2. All physical parameters were estimated based on a distance of 2.5 kpc. The CO clouds are at the same distance since they have similar radial velocities around $\sim -35 \text{ km s}^{-1}$. We see that there are no broad-line features with velocity-widths above 10 km s^{-1} in the CO spectra. In order to estimate the mass of the CO clouds M_{cloud} , we used the following equation:

$$M_{\text{cloud}} = \mu m_{\text{H}} \sum_i [D^2 \Omega N_i(\text{H}_2)], \quad (1)$$

where μ is the mean molecular weight, m_{H} is the mass of the atomic hydrogen, D is the distance to the CO cloud, Ω is the solid angle of a square pixel, and $N_i(\text{H}_2)$ is the hydrogen column density of each pixel i in the Galactic longitude-latitude plane. We used $\mu = 2.8$ to account for a helium abundance of 20 %. The hydrogen column density $N(\text{H}_2)$ is derived by using the relationship

$$X = N(\text{H}_2)/W(^{12}\text{CO}), \quad (2)$$

where X is an X-factor in units of $\text{cm}^{-2} (\text{K km s}^{-1})^{-1}$. We used $X = 2.0 \times 10^{20}$ in the present paper (Bertsch et al. 1993). We estimated the total mass of the CO clouds to be at least $\sim 6,500 M_{\odot}$.

3.2. Physical Conditions of Molecular Gas

In order to investigate the physical conditions of the associated CO clouds, we have calculated the line intensity ratio map using the $^{12}\text{CO}(J=2-1)$ and $^{12}\text{CO}(J=1-0)$ emission lines. The intensity ratio corresponds to the degree of the rotational excitation of molecules, which reflects the gas density and/or temperature. Both datasets were smoothed to an angular resolution of ~ 180 arcsec (FWHM) and summed up to 1 km s^{-1} per velocity bin. The data points used for the analysis were those above the 3σ noise level in both lines.

Figure 4 shows the velocity channel distributions of the line intensity ratio $^{12}\text{CO } J=2-1/1-0$ every 3 km s^{-1} .

TABLE 2
PHYSICAL PROPERTIES OF $^{12}\text{CO}(J = 1-0)$ CLOUDS

Name	Position	l (deg)	b (deg)	T_R^* (K)	V_{peak} (km s^{-1})	ΔV_{LSR} (km s^{-1})	$N_{\text{p}}(\text{H}_2)$ ($\times 10^{21} \text{ cm}^{-2}$)	Size (pc)	Mass (M_{\odot})	Associated
(1)	(2)	(3)	(4)	(5)	(6)	(7)	(8)	(9)	(10)	(11)
CO -37 E	A	315.57	-2.52	6.9	-35.5	2.2	5.7	12.4	3699	Yes
	B	315.56	-2.47	4.2/3.5	-35.7/-37.6	2.0/2.8	5.8			
	C	315.73	-2.40	5.6	-36.3	2.4	5.3			
CO -35 SE	D	315.43	-2.70	2.0	-34.7	1.6	3.4	5.1	170	Yes
CO -33 S	E	315.22	-2.73	2.7	-33.7	4.6	4.6	>8.6	>1520	Yes
	F	315.17	-2.78	3.8	-30.8	3.0	4.5			
CO -40 NW	G	315.36	-1.93	1.9	-35.8	1.3	1.9	>9.0	>1070	Yes
	H	315.28	-1.92	2.6	-43.0	2.4	2.9			
CO -55 N	I	315.36	-2.10	3.3	-55.1	1.7	1.9			No
CO -48 NE	J	315.70	-2.23	1.6	-47.5	1.9	1.1			No
CO -57 SW	K	315.02	-2.25	5.2	-56.7	2.0	3.8			No
CO -5 SW	L	314.93	-2.32	4.5	-4.5	0.8	1.4			No

NOTE. — Col. (1): Cloud name. Col. (2): Position name. Cols. (3–4): Position of the maximum CO intensity for each velocity component. Cols. (5–8): Physical properties of the $^{12}\text{CO}(J = 1-0)$ emission obtained at each position. Col. (5): Peak radiation temperature, T_R^* . Col. (6): V_{peak} derived from a single Gaussian fitting. Col. (7): Full-width half-maximum (FWHM) line width, ΔV_{peak} . Col. (8): Proton column density $N_{\text{p}}(\text{H}_2)$ derived from the CO integrated intensity, $W(^{12}\text{CO})$, $N(\text{H}_2) = 2 \times 10^{20} [W(^{12}\text{CO})/(\text{K km s}^{-1})] (\text{cm}^{-2})$ (Bertsch et al. 1993). Col. (9): Cloud size defined as $(A/\pi)^{0.5} \times 2$, where A is the total cloud surface area surrounded by the 3σ levels in the integrated intensities of each CO cloud. Col. (10): Mass of the cloud derived using the relation between the molecular hydrogen column density $N(\text{H}_2)$, and the $^{12}\text{CO}(J = 1-0)$ integrated intensity, $W(^{12}\text{CO})$, shown in Col. (8).

We found that part of the CO -37 E cloud shows an intensity ratio significantly higher than 0.8 (Figure 4c), while the region in the immediate vicinity of the cloud shows values smaller than 0.6 (Figures 4c, 4d, and 4e). This may be due to some external influences that affect only the surface of the clouds because an intensity ratio of < 0.6 is typical of dark molecular clouds in the Milky Way without extra heating (e.g., Sakamoto et al. 1997). In addition to the CO -37 E cloud, we note that the edges of the CO -40 NW, CO -35 SE, and CO -33 S clouds also have intensity ratios higher than 0.8. Figures 4a', b', and d' show the line intensity ratio maps toward these clouds superposed with the same radio continuum contours as in Figure 1. The regions having intensity ratios higher than 0.8 are located along the radio shell of RCW 86. This is not considered to be due to stellar feedback since there are no *IRAS/AKARI* infrared point sources or OB type stars in these regions (e.g., Westerlund 1969; Helou & Walker 1988; Ishihara et al. 2010). Therefore, this enhanced ratio indicates shock heating/compression due to the forward shock and/or stellar winds from the progenitor of RCW 86, which supports the association between the SNR and the CO clouds.

3.3. Expanding Structure and Physical Properties of HI and CO

Figure 5a shows the HI velocity-latitude diagram. The integration range in Galactic longitude is from 315°48 to 315°56, as shown in Figure 2. We found an HI cavity-like structure in the radial velocity range from -46 to -28 km s^{-1} , which has a size similar to RCW 86 in terms of the Galactic latitude range (~ 40 arcmin; ~ 30 pc at the distance of 2.5 kpc). The large velocity range involved, nearly 20 km s^{-1} , cannot be explained by the Galactic rotation. We suggest that this feature represents an expanding structure driven by the stellar feedback of the progenitor of RCW 86. The HI expanding motion was also seen in the velocity channel distribution from -45 to -25 km s^{-1} (see Appendix Figure A.1) and

the HI line profile in Figure 5b. We also show the $^{12}\text{CO}(J = 2-1)$ contours in black. At $b > -2^\circ 5$, the CO cloud has velocities higher (from -40 to -35 km s^{-1}) than the rest of the CO cloud, at $b < -2^\circ 5$, for which velocities span from -37 to -32 km s^{-1} .

The bright region of the HI image is shifted toward the center of the SNR with a velocity increase from -45 to -25 km s^{-1} . We interpret that the HI components of -46 km s^{-1} and -28 km s^{-1} correspond to the blue- and red-shifted sides of the expanding HI wall, respectively. We note that the HI intensity of the red-shifted side is approximately twice as high as that of the blue-shifted side. If the emission is optically thin, the HI intensity corresponds to the mass. By assuming this inhomogeneous gas distribution, the central velocity, V_{center} , and expansion velocity, ΔV , were estimated to be $V_{\text{center}} \sim -35$ km s^{-1} and $\Delta V \sim 7$ –11 km s^{-1} , respectively. Here the central velocity corresponds to the kinematic distance of $\sim 2.4 \pm 0.2$ kpc adopting the Galactic rotation curve model of Brand & Blitz (1993). The error was derived using the uncertainty in the central velocity intrinsic to this method. The estimated distance is consistent with previous studies (e.g., Westerlund 1969; Rosado et al. 1996; Helder et al. 2013; Ajello et al. 2016). The total mass and mean density of neutral atomic gas are estimated to be $\sim 2 \times 10^4 M_{\odot}$ and $\sim 70 \text{ cm}^{-3}$, where the shell radius and thickness are assumed to be ~ 15 pc and ~ 5 pc, respectively (c.f., H. E. S. S. Collaboration et al. 2016). HI gas is generally considered to be optically thin (optical depth $\tau \ll 1$), having a column density, $N_{\text{p}}(\text{HI})'$ (e.g., Dickey & Lockman 1990):

$$N_{\text{p}}(\text{HI})' = 1.823 \times 10^{18} \int T_{\text{L}}(V) dV (\text{cm}^{-2}), \quad (3)$$

where $T_{\text{L}}(V)$ is the observed HI brightness temperature in units of K. On the other hand, according to Fukui et al. (2015), 85 % of HI gas is optically thick ($\tau \sim 0.5$ –3) in the Milky Way, and the averaged column density is approximately 2–2.5 times higher than

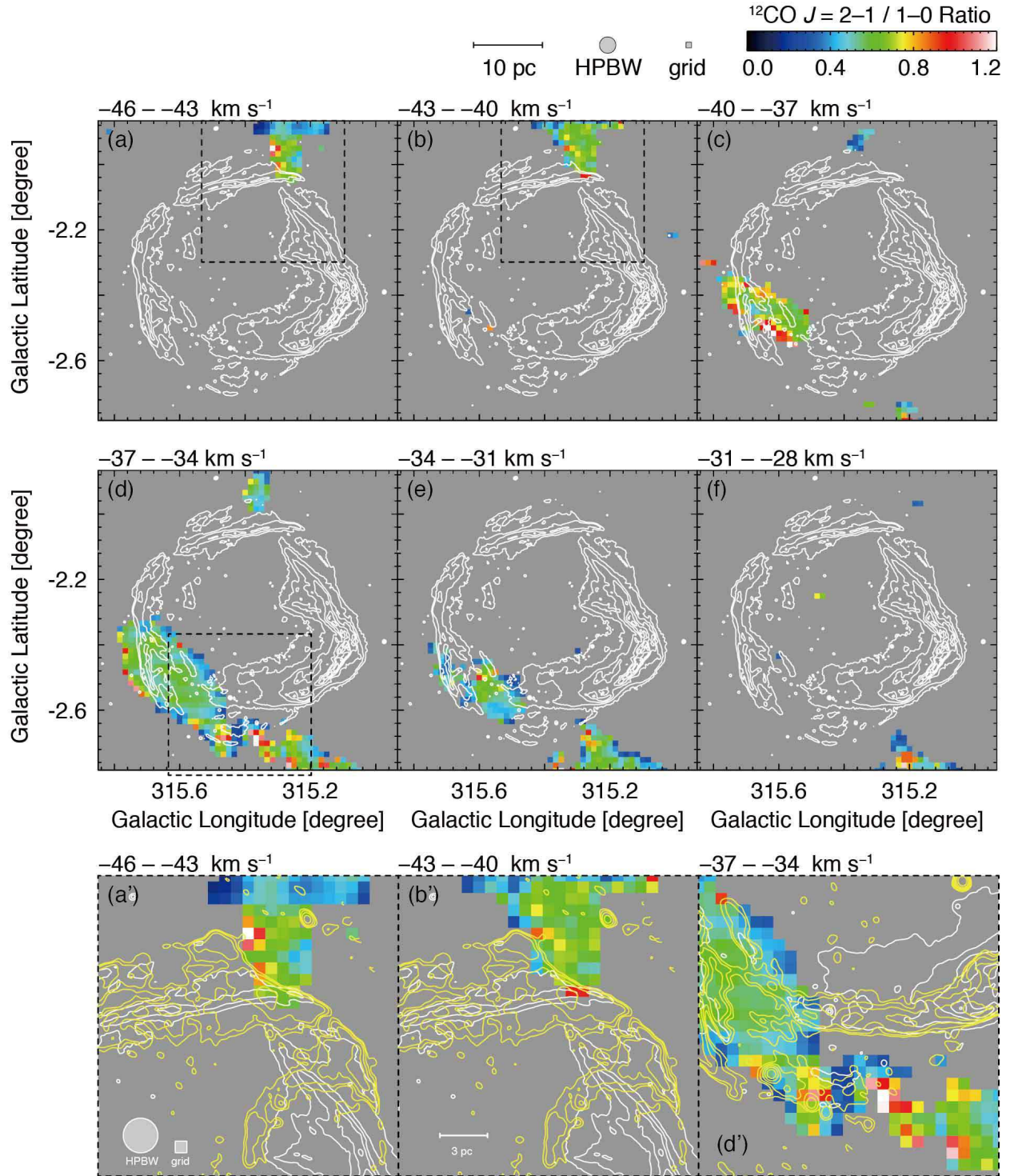


FIG. 4.— (a–f) Velocity channel maps of the line intensity ratio $^{12}\text{CO } J = 2-1/1-0$ at an interval of 3 km s^{-1} in a velocity range from -46.0 to -28.0 km s^{-1} . The white contours show the X-ray intensity distributions shown in Figure 3. (a', b', d') Enlarged views toward dashed regions in Figures 4a, b, and d. The yellow contours indicate the MOST radio continuum at a frequency of 843 MHz. The contour levels are 2.5, 5, 10, 20, 40, 80, and $160 \text{ mJy beam}^{-1}$.

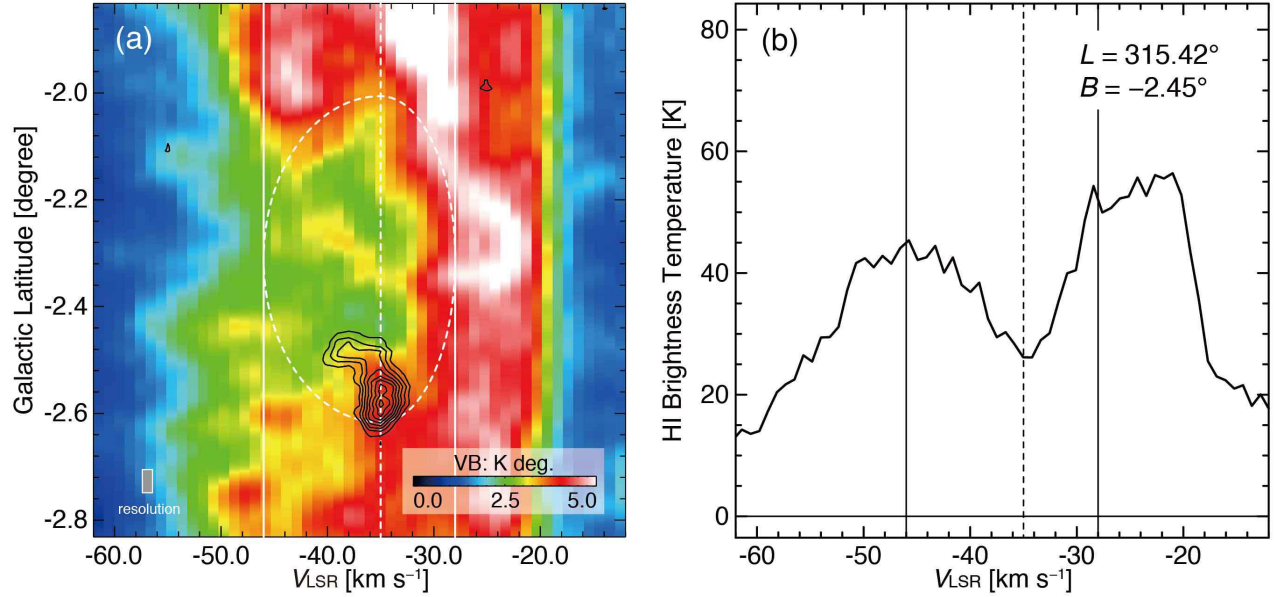


FIG. 5.— (a) Velocity-Latitude diagram of HI. The integration range in Galactic longitude is from $315^\circ 48$ to $315^\circ 56$, as shown in Figure 2. Black contours indicate the intensity distribution of $^{12}\text{CO}(J=2-1)$. The lowest contour level and intervals are 0.03 K degree and 0.02 K degree, respectively. Dashed circle and vertical solid lines show an asymmetrically expanding spherical shell and the velocity integration range of Figure 2. (b) HI spectra at $(l, b) = (315^\circ 42, -2^\circ 45)$. Velocity range and vertical lines are the same as Figure 5a.

that derived on the optically thin assumption described by equation (3). Subsequently, the authors established a more accurate relationship under consideration of the dust growth model (Fukui et al. 2017 in preparation). Therefore, we used the following relationship to calculate the “true” HI column density, $N_p(\text{HI})$, instead of equation (3):

$$N_p(\text{HI}) = S \times N_p(\text{HI})' (\text{cm}^{-2}), \quad (4)$$

where S is the conversion factor from $N_p(\text{HI})'$ to $N_p(\text{HI})$. In the region around RCW 86, the conversion factor, S , is estimated to be 2.3. Unless otherwise noted, we used equation (4) and $S = 2.3$ to calculate the HI column density in this article. In the SNR RCW 86, $N_p(\text{HI})$ is accurately determined within $\sim 8\%$, while the integrated intensity of HI varies from 600 to 1,000 K km s^{-1} .

3.4. Detailed Comparison with X-rays

In order to establish a more detailed correspondence between the ISM and X-ray filaments in the velocity range from -46 km s^{-1} to -28 km s^{-1} , we compare the integrated CO/HI intensity map with the thermal and non-thermal X-rays.

Figure 6 shows the intensity distribution of thermal X-rays, HI, and CO. The $\text{H}\alpha$ contours with 500 dR or higher are also shown in the upper left of Figure 6. We focused on the eastern, northern, and southwestern regions where thermal X-rays show filamentary distributions. In the eastern region the thermal X-ray filaments are distributed along with the CO -37°E cloud. The X-ray distribution cannot be interpreted by interstellar photoelectric absorption of the low-energy X-rays, because the thermal X-rays are not superposed onto the intensity peak of the CO cloud. We also found that the

X-ray filament TX-E1 complex $(l, b) \sim (315^\circ 68, -2^\circ 46)$ is slightly aligned with the CO clumpy structure, while another filament TX-E2 complex, $(l, b) \sim (315^\circ 60, -2^\circ 55)$, is not much correlated with the CO cloud. This trend suggests that the degree of interaction between the SNR shocks and the CO cloud is different between the two regions. In the northern and southwestern regions, the distribution of the thermal X-rays shows a good spatial correlation with that of the HI cavity wall at a scale of $\sim 1 \text{ pc}$, where the HI intensity is significantly increased outwards from the SNR.

Figure 7 shows the radial profiles of the proton column density $N_p(\text{HI})$ (gray filled areas) and the thermal X-ray intensity (red) for each region of dashed rectangles, perpendicular to the shell as shown in Figure 6. Each region has a $670'' \times 160''$ size corresponding to $8 \text{ pc} \times 2 \text{ pc}$, and is centered on the X-ray filament (see Table 3). We defined the origin of the radial profile as the position of the maximum X-ray intensity in the projected distance. Positive and negative values correspond to the outer and inner sides of the SNR shell, respectively. The regions are selected every $\sim 3 \text{ pc}$ relative to the azimuthal direction, and all of them cross local X-ray peaks. We also added the $\text{H}\alpha$ distribution (light blue) in the TX-N2, TX-SW1, and TX-SW2 regions, which have $\text{H}\alpha$ fluxes of 500 dR or higher. The intensity scales of the thermal X-rays and $\text{H}\alpha$ are normalized by their maximum values, and the positions of the intensity peaks are indicated by the vertical dashed lines. We find that the positions of the HI intensity peaks correspond well with those of X-rays and $\text{H}\alpha$, except in TX-SW1. In order to evaluate quantitatively this trend, we estimated the accurate values of intensity peaks on the radial profiles. Table 3 shows a summary of the radial profile towards each thermal X-ray peak. We defined the separation from the X-ray intensity peak to the HI or $\text{H}\alpha$ intensity peaks in the radial distribution, in

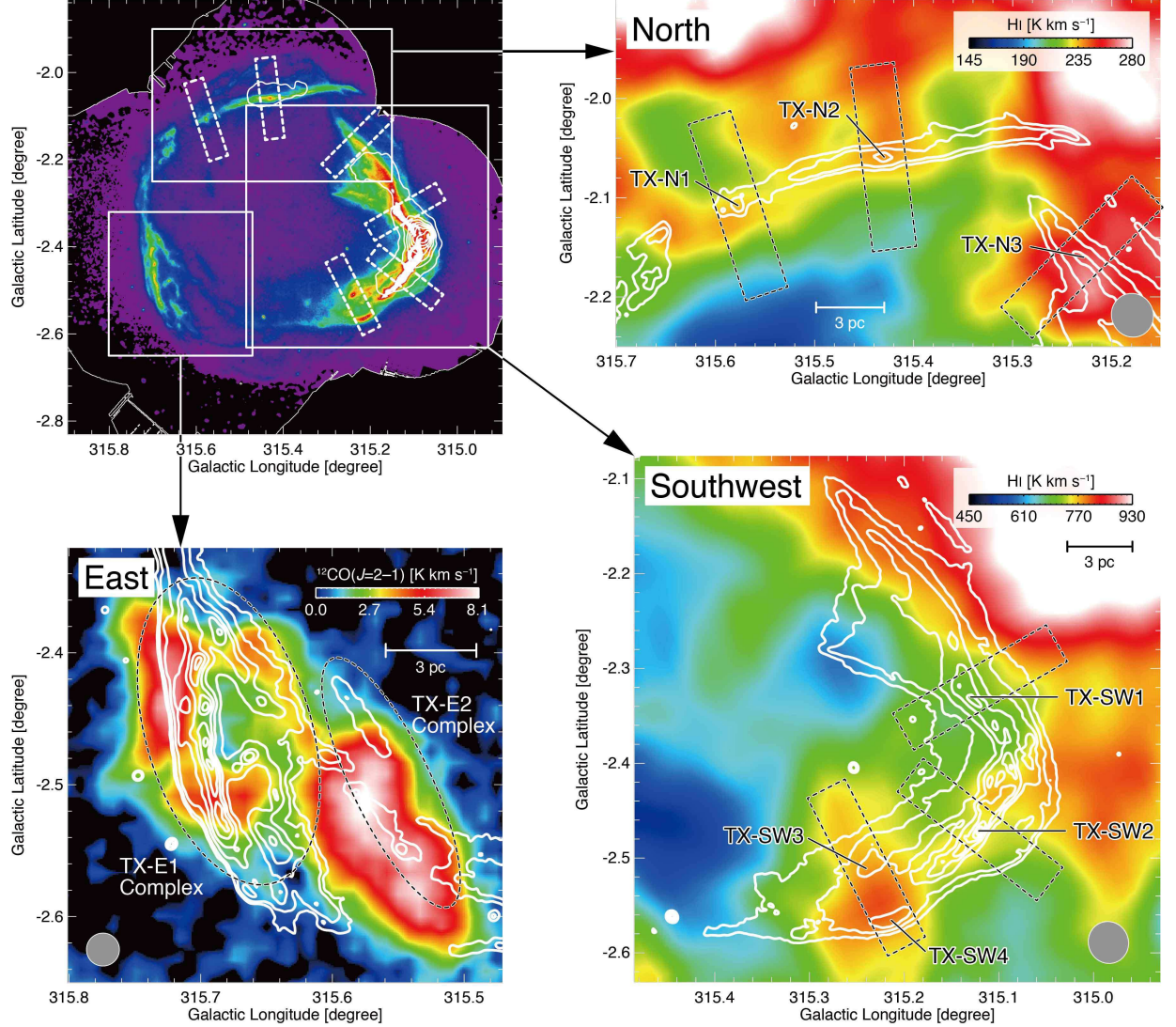


FIG. 6.— Top left: *XMM-Newton* X-ray image in the energy band of 0.5–1.0 keV overlaid with the $H\alpha$ intensity contours (lowest: 500 dR, interval: 250 dR) taken from SHASSA (Gaustad et al. 2001). Other panels: Distributions of HI and $^{12}\text{CO}(J=2-1)$ obtained with ATCA & Parkes and NANTEN2 (rainbow scale) superposed with the *XMM-Newton* X-ray contours in the energy band of 0.5–1.0 keV. The three regions toward the north, east, and southwest are shown with inserts in the X-ray image on the top left panel. The velocity range spans from -32 to -29 km s^{-1} in the north; from -36 to -34 km s^{-1} in the east; and from -42 to -28 km s^{-1} in the southwest. The contour levels of the X-rays are 6.00×10^{-5} , 1.42×10^{-4} , 3.87×10^{-4} , 7.95×10^{-4} , 1.37×10^{-3} , 2.10×10^{-3} , and 3.00×10^{-3} photons $\text{s}^{-1} \text{pixel}^{-1}$ for the north and the southwest; 2.50×10^{-5} , 3.54×10^{-5} , 6.67×10^{-5} , 1.19×10^{-4} , 1.92×10^{-4} , 2.85×10^{-4} , and 4.00×10^{-4} photons $\text{s}^{-1} \text{pixel}^{-1}$ for the east.

such a way that a positive (negative) value implies that the X-ray peak lies to the left (right) of the other peaks in the diagram. The separations between the thermal X-ray peak and the HI/ $H\alpha$ peaks are smaller than the beam size of the HI data, ~ 156 arcsec, except for the HI peak of TX-SW1.

We also estimated the mean HI column density $\langle N_p(\text{HI}) \rangle$ within each rectangle. The double-logarithm plot in Figure 8 shows the correlation between $\langle N_p(\text{HI}) \rangle$ and the peak intensity of the thermal X-rays. The solid line shows the linear regression by least-squares fitting, with a correlation coefficient of ~ 0.76 . We conclude that the thermal X-ray intensity increases following roughly a power-law dependence with the column density of neutral atomic gas at a pc scale.

Figure 9 shows the intensity distribution of the non-thermal X-rays and HI. We focused on the northern, southwestern, and northeastern regions, where non-thermal X-rays are prominent. In the northern and southwestern regions, the non-thermal X-ray filaments are spatially well correlated with the HI bright-rim at a pc scale, as well as the thermal X-rays in Figure 7. In contrast, the X-ray peaks NTX-NE1 and NTX-SW5 are located inside the HI bright wall, while the shape of NTX-NE1 filament slightly matches the HI distribution. In addition to this, we also find that the non-thermal X-ray complex of NTX-NE4, $(l, b) \sim (315^\circ 57, -2^\circ 24)$, is located inwards with respect to NTX-NE1, while the NTX-SW6 complex, $(l, b) \sim (315^\circ 44, -2^\circ 66)$, lies outwards from NTX-SW5.

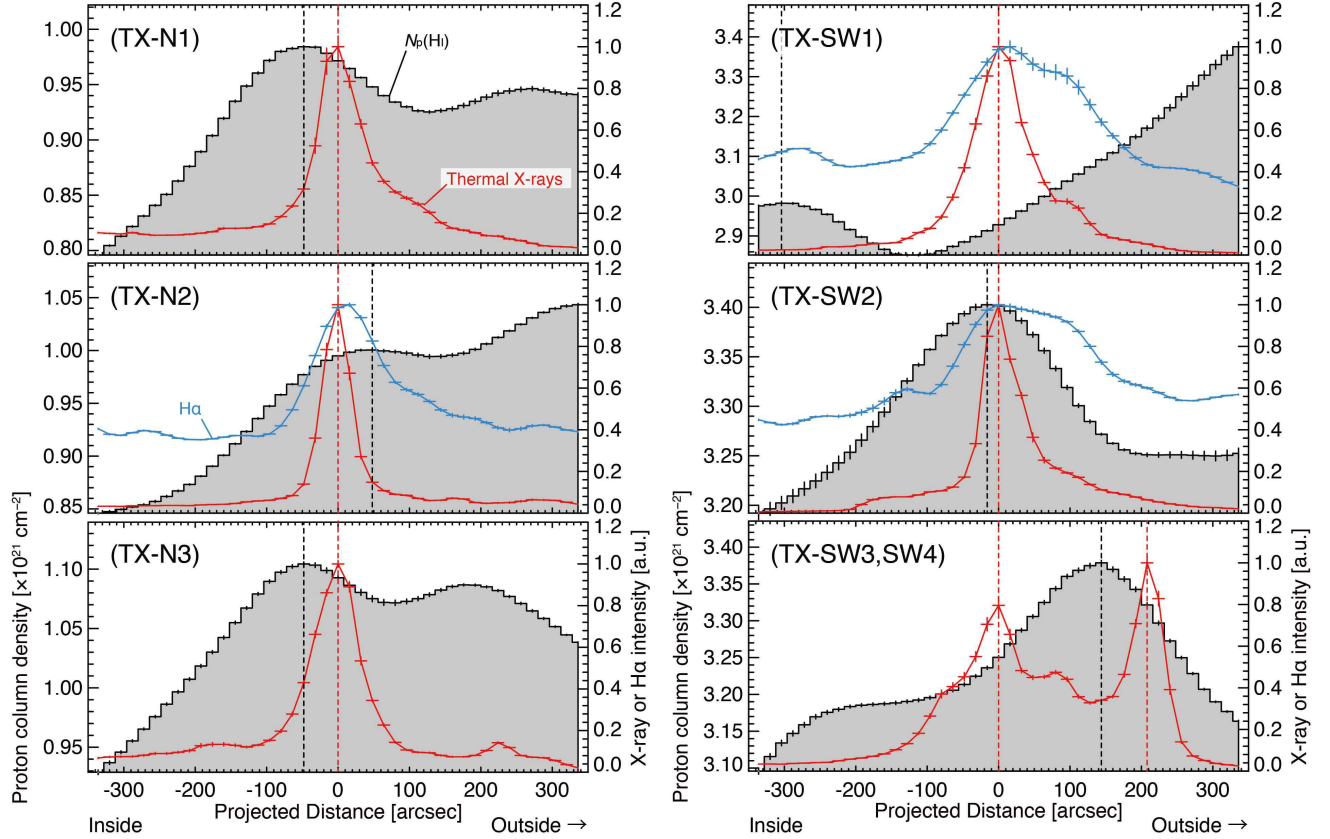


FIG. 7.— Radial Profiles of the atomic proton column density $N_p(\text{HI})$ (gray filled areas), thermal X-rays (red), and $\text{H}\alpha$ emissions (light blue) for each rectangle region as shown by Figures 6. Black, red, and light-blue dashed lines indicate the intensity peaks of $N_p(\text{HI})$, thermal X-rays, and $\text{H}\alpha$, respectively.

TABLE 3
RESULTS OF THE PROJECTED PROFILE TOWARDS THE THERMAL X-RAY PEAKS

Name (1)	Thermal X-rays			$\langle N_p(\text{HI}) \rangle$ ($\times 10^{21} \text{ cm}^{-2}$) (5)	Separation	
	l (deg) (2)	b (deg) (3)	Peak Intensity ($\times 10^{-4} \text{ counts s}^{-1} \text{ pixel}^{-1}$) (4)		HI Peak (arcsec) (6)	H α Peak (arcsec) (7)
TX-N1	315.58	-2.11	1.30 ± 0.07	0.92 ± 0.05	-48	—
TX-N2	315.43	-2.06	3.79 ± 0.11	0.96 ± 0.07	+32	16
TX-N3	315.23	-2.16	3.94 ± 0.07	1.05 ± 0.05	-48	—
TX-SW1	315.14	-2.32	12.6 ± 0.3	3.03 ± 0.15	-304	16
TX-SW2	315.12	-2.47	20.6 ± 0.8	3.29 ± 0.06	-16	0
TX-SW3	315.24	-2.51	4.8 ± 0.2	3.24 ± 0.08	+144	—
TX-SW4	315.22	-2.57	6.0 ± 0.2	3.24 ± 0.08	-68	—

NOTE. — Col. (1): X-ray peak name. Cols. (2–4): Physical properties of the thermal X-rays. Cols. (2–3): Position of the X-ray peak. Col. (4): Peak intensity of the X-ray. Col. (5): Mean HI column density, $\langle N_p(\text{HI}) \rangle$, within each region shown by Figure 6. Col. (6): Separation between each intensity peak of the X-ray and HI emissions. Col. (7): Separation between each intensity peak of the X-ray and $\text{H}\alpha$ emissions.

We analyzed each non-thermal X-ray peak in a manner similar to the thermal X-ray case. Figure 10 shows the radial profiles of the proton column density, $N_p(\text{HI})$ (gray filled areas), and non-thermal X-ray intensity (green) for each rectangle, as shown by Figure 9. Here, we considered the column density of the molecular hydrogen, $N(\text{H}_2)$, toward the NEX-NE2, -NE3 region, where there is a significant amount of molecular mass. Finally, we estimated the total proton column density, $N_p(\text{H}_2 + \text{HI})$, by

$$N_p(\text{H}_2 + \text{HI}) = 2 \times N(\text{H}_2) + N_p(\text{HI}), \quad (5)$$

We also added the radio continuum distribution (blue) in all the regions. The difference in the distributions of the non-thermal X-rays and the radio continuum indicate the energy difference of the CR electrons. The X-ray and radio peaks are located around the HI intensity peaks. We did not find a specific trend among them, such as the correlation between X-rays and HI. The position of the

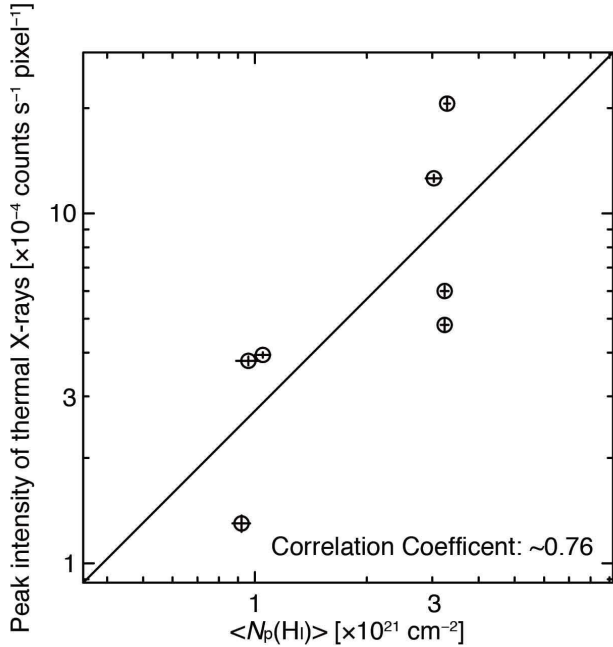


FIG. 8.— Correlation plot between the averaged HI column density $\langle N_p(\text{HI}) \rangle$, and the peak intensity of thermal X-rays. The error bars are also indicated. The solid line shows the linear regression of the double logarithm plot applying a least squares fit, where the correlation coefficient is ~ 0.76 .

intensity peaks is represented by the vertical dashed lines of both the X-ray and radio peaks. We note that the relative radial positions between the X-ray and radio peaks show significant offsets from each other. Specifically, the non-thermal X-ray intensity peaks NTX-N1–N4, NTX-NE1, and NTX-SW2 are positioned farther outside than the nearest radio peaks, while the NTX-NE2–3, NTX-SW1, and NTX-SW3–5 peaks are located farther inside than the nearest radio peaks. Table 4 shows the trend quantitatively. The positive (negative) values of the separation correspond to the case in which the non-thermal X-ray intensity peaks are positioned inwards (outwards) from the nearest radio peaks. Most of the separations are larger than half of the beam size for both the radio and X-rays ($\Delta\theta \sim 20$ arcsec). Considering the extended radial distribution of the radio peaks, all the separations are regarded to be significant. Figure 11 shows a logarithmic plot of the correlation between the averaged total proton column density $\langle N_p(\text{H}_2 + \text{HI}) \rangle$ and the peak intensity of the non-thermal X-rays. Filled circles represent positive separations, while open triangles are used to plot negative ones. The vertical dashed line indicates $\langle N_p(\text{H}_2 + \text{HI}) \rangle = 1 \times 10^{21} \text{ cm}^{-2}$. In contrast to the thermal X-ray case, there is no significant correlation between the non-thermal X-rays and $\langle N_p(\text{H}_2 + \text{HI}) \rangle$: if a least-square fitting is attempted to the double logarithm plot, the correlation coefficient turns out to be ~ 0.03 . We find that, with the only exception of NTX-SW2, the negative separations are clustered within the low-density region ($\sim 1 \times 10^{21} \text{ cm}^{-2}$), whereas the positive separations are only located in regions of density higher than $\sim 3 \times 10^{21} \text{ cm}^{-2}$.

4. DISCUSSION

4.1. Progenitor System of RCW 86

There have been considerable debates on the progenitor system (CC or Type Ia) of RCW86 since its discovery (Westerlund 1969; Claas et al. 1989; Kaastra et al. 1992; Vink et al. 1997; Bamba et al. 2000; Yamaguchi et al. 2011; Williams et al. 2011; Broersen et al. 2014). Recent multi-wavelength observations as well as theoretical studies in the last several years reveal the progenitor is a Type Ia SN. Ueno et al. (2007) and Yamaguchi et al. (2008) found that the abundant Fe ejecta and the absence of rich O ejecta are consistent with a Type Ia SNR. Williams et al. (2011) argued that the $\text{H}\alpha$ filamentary distributions are created by the interaction between the SNR shocks and the neutral gas and suggested that the interaction between the SNR shock and the ambient gas was weak (e.g., Chevalier et al. 1980; Smith 1997). This is consistent with the accretion wind by a Type Ia progenitor (e.g., Hachisu et al. 1996; Nomoto et al. 2007). A central compact stellar remnant like a neutron star or a pulsar wind nebula is not yet detected, again favoring a Type Ia (e.g., Kaplan et al. 2004). Williams et al. (2011) calculated an off-center explosion by using a 2D hydrodynamic model, applying parameters given by the Type Ia progenitor accretion wind model proposed by Badenes et al. (2007). The authors showed that the size of the SNR, shock-velocity, and post-shock gas density are well reproduced, concluding that RCW 86 is Type Ia explosion in an accretion-wind bubble. In this section we discuss the progenitor system of RCW 86 based on the results of the associated interstellar gas.

First, we shall argue that the HI/CO expanding structure is inconsistent with the acceleration by only the accretion wind of the progenitor. The expansion velocity of HI $\sim 7 \text{ km s}^{-1}$ in the red-shifted (gas-rich) side and the total HI mass $2 \times 10^4 M_\odot$ lead to a momentum of $\sim 3 \times 10^{38} \text{ N}\cdot\text{s}$ for the HI shell. Figure 5a shows that the CO peak velocity is shifted by $\sim 3 \text{ km}$ towards the interior of the SNR. The momentum of this shifted component is only 5 % of the whole CO –37 E cloud and the CO kinetic energy is negligible as compared to the HI kinetic energy. Hachisu et al. (1996) showed that the accretion wind of a Type Ia progenitor has a typical duration of $3 \times 10^5 \text{ yr}$, where the wind mass and wind velocity are $\sim 10^{-6} M_\odot \text{ yr}^{-1}$ and $\sim 1,000 \text{ km s}^{-1}$, respectively. This means that the momentum released by the accretion wind amounts to $\sim 6 \times 10^{35} \text{ N}\cdot\text{s}$, which is quite small to explain the observed momentum of the HI shell. Moreover, it is difficult to explain the shell formation in terms of the SN shock waves. RCW 86 has an age of $\sim 1,800 \text{ yr}$ and the duration of the shock interaction with the ambient medium is too short to transfer the momentum significantly. This is consistent with the absence of wing like emission spanning more than 10 km s^{-1} in the CO spectra (e.g., Seta et al. 1998; Yoshiike et al. 2013) and the fact that only a thin surface of CO gas is heated by shock interaction (see also Figure 4). The short duration of the interaction is also suggested from the X-ray spectroscopy. Vink et al. (1997) showed that the thermal plasma in RCW 86 is dramatically deviated from the thermal equilibrium and noted that there is a spot of extremely short ionization timescale in the SNR. In particular, the time elapsed since the Fe ejecta was heated by the reverse SNR shock is estimated to be $< 380 \text{ yr}$,

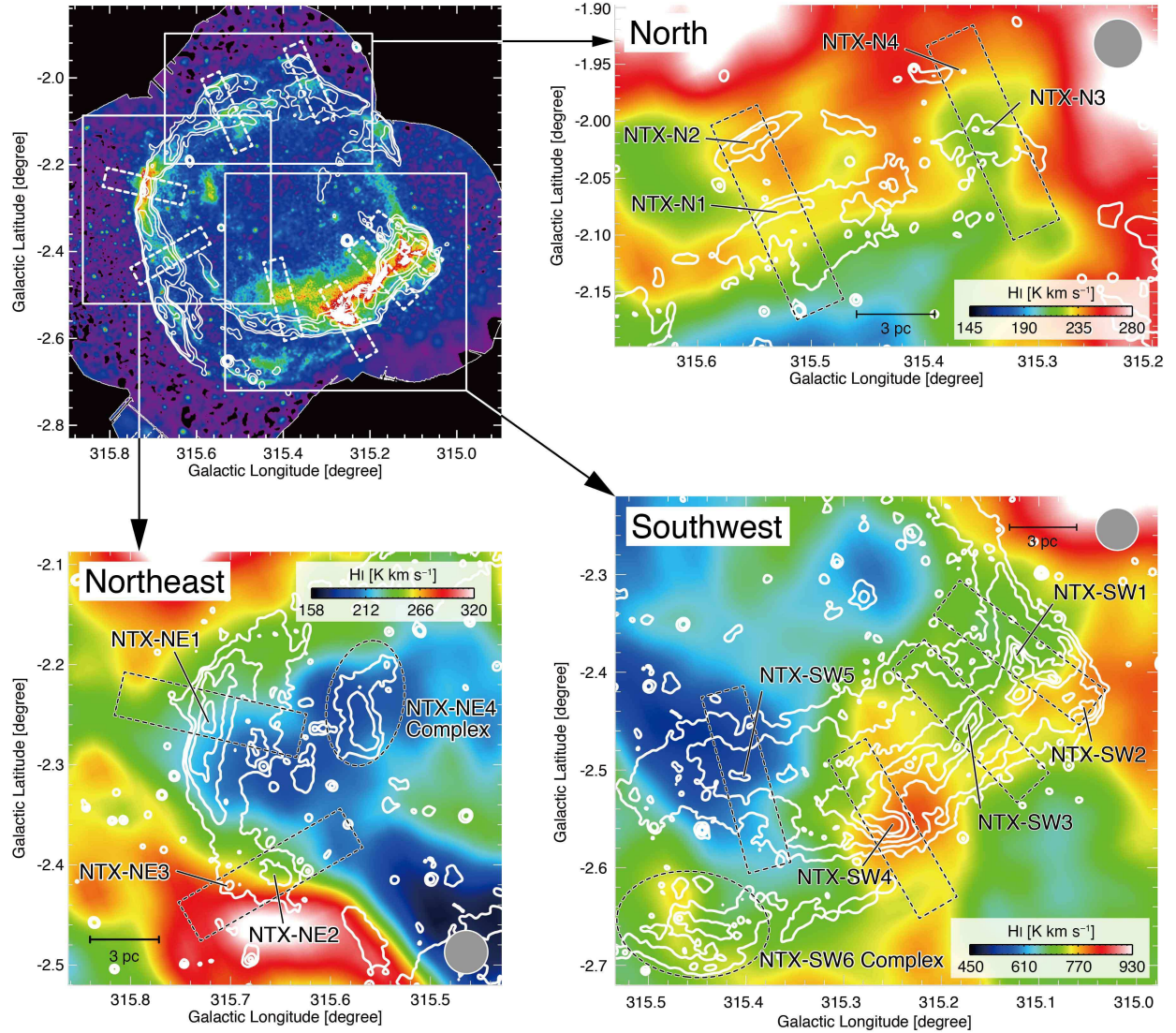


FIG. 9.— Top left: *XMM-Newton* X-ray image in the energy band of 2.0–4.5 keV overlaid with MOST radio continuum contours as shown in Figure 1. Other three panels: distributions of HI obtained with ATCA & Parkes (rainbow scale) superposed with the *XMM-Newton* X-ray contours in the energy band of 2.0–4.5 keV. The three regions toward the north, the northeast, and the southwest are shown with inserts in the X-ray image on the top left panel. The velocity range spans from -32 to -29 km s $^{-1}$ in the north; from -38 to -33 km s $^{-1}$ in the northeast; and from -42 to -28 km s $^{-1}$ in the southwest. The contour levels of the X-rays are 8.0×10^{-8} , 1.7×10^{-8} , 4.4×10^{-5} , 8.8×10^{-5} , and 1.5×10^{-4} photons s $^{-1}$ pixel $^{-1}$.

a fourth of the SNR age (e.g., Yamaguchi et al. 2008). We suggest that the HI/CO expanding structure could be formed by the stellar winds from nearby OB stars (e.g., Westerlund 1969). Figure 12 shows that RCW 86 is at the inner edge of a molecular supershell created by multiple supernova remnants in the Galactic plane. The expansion in RCW 86 may originate in the supershell.

Comparison with other CC SNRs of similar ages and properties reinforces that RCW 86 is a Type Ia SNR with a low-velocity wind. Because of their similarities, RX J1713.7–3946, a CC shell SNR with an age of $\sim 1,600$ years, emitting bright TeV γ -ray and non-thermal X-rays (Fukui et al. 2003; Cassam-Chenaï et al. 2004; Moriguchi et al. 2005), is the best target to compare with RCW 86. In RX J1713.7–3946, molecular clouds of $n > 10^4$ cm $^{-3}$ remained without being swept up by the SNR

shock wave, whereas the intercloud and diffuse HI gas were evacuated by the strong stellar winds from the massive progenitor (e.g., Fukui et al. 2003; Moriguchi et al. 2005; Sano et al. 2010, 2013; Maxted et al. 2013). As a result, in RX J1713.7–3946 we do not see the HI envelope of CO clouds and strong thermal X-rays are not detected (e.g., Takahashi et al. 2008; Fukui et al. 2012; Sano et al. 2015). In RCW 86, instead, we see diffuse HI toward the CO clouds. In particular, we can clearly see an HI envelope around CO -37° E (see Figure 2). This suggests that the progenitor had a weaker wind than the massive progenitor of the CC SNR RX J1713.7–3946 and is consistent with the accretion wind hypothesis. The CC scenario with an early B-star, nevertheless, cannot be ruled out. The thermal X-rays observed over the whole RCW 86 suggest that a large amount of HI gas is distributed

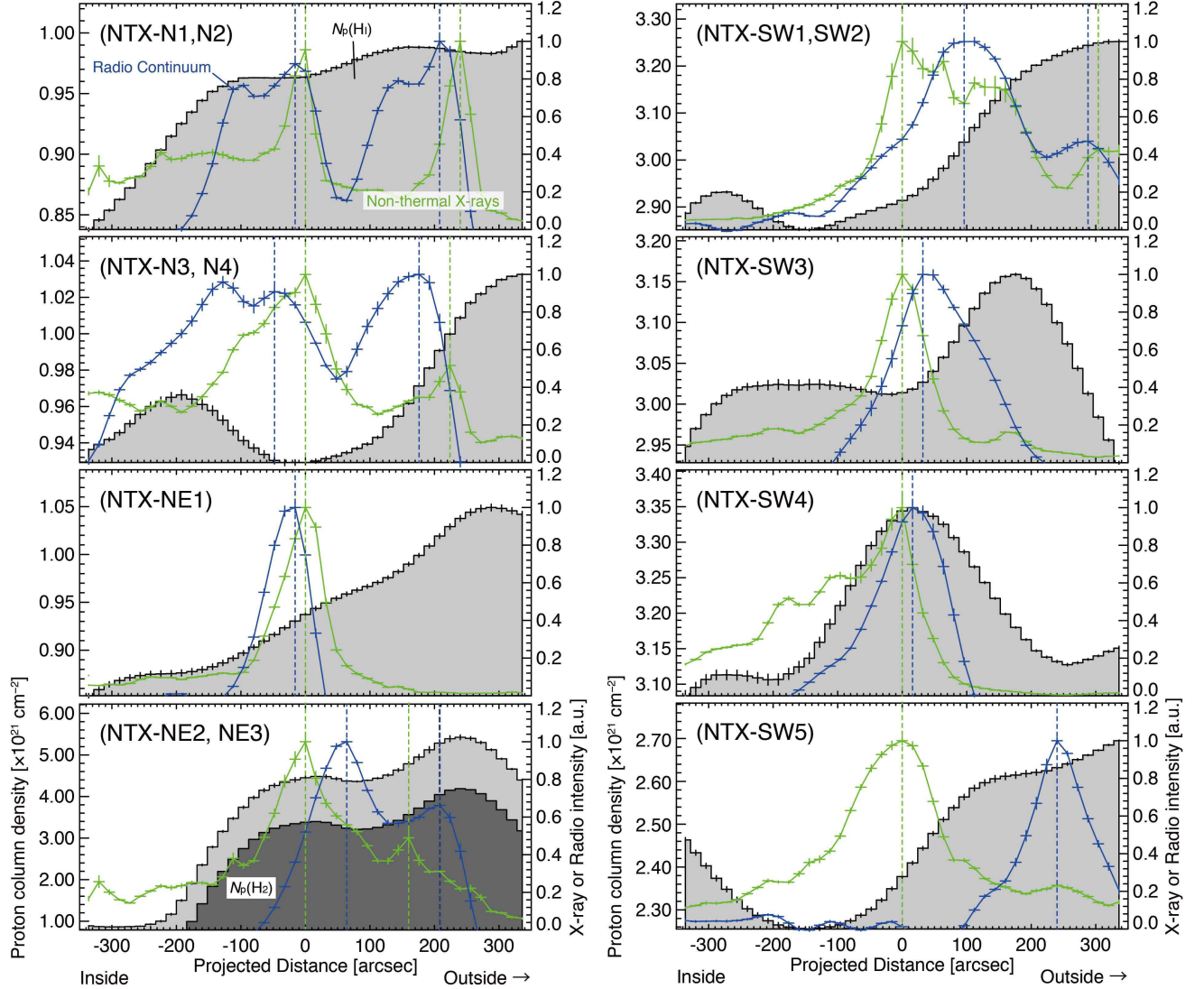


FIG. 10.— Radial profiles of proton column density (black), non-thermal X-rays (green), and radio continuum (blue) for each rectangle region, as shown by Figures 9. Gray and black filled areas represent the atomic proton column density, $N_p(\text{H I})$, and the molecular proton column density, $N_p(\text{H}_2)$, respectively. Green and blue dashed lines indicate the intensity peaks of non-thermal X-rays and radio continuum radiation, respectively.

inside the shell.

These thermal X-rays are produced by the interaction of shock waves with the preexistent neutral and ionized gas, even though observational evidence for the interaction was not obtained (e.g., Rho et al. 2002; Yamaguchi et al. 2011). Figure 7 shows that the thermal X-ray peaks coincide with the H I peaks, indicating that the shock waves have collided into the H I cavity-wall and radiate the thermal X-rays. Only in TX-S1 the H I does not coincide with the X-ray peak. This difference is explained if we assume that the H I associated with TX-S1 is already ionized, because the X-rays peak at the H α peak and the electron density is estimated to be $\sim 100 \text{ cm}^{-3}$ in the South (Ruiz 1981). In addition, the intensity of the thermal X-rays increases with the neutral gas density, suggesting that the gas is thermalized by the shock passage. Detailed spectrum analysis of X-rays comparable to the interstellar distribution will reveal a better

correlation between the proton column density and thermal X-ray intensity. Based on the considerations above, we conclude that RCW 86 is the remnant of a Type Ia explosion in a wind-bubble and state that a thorough investigation of the neutral gas is an important tool to investigate the progenitor system and the origin of the thermal X-rays.

4.2. Efficient CR Acceleration

Sano et al. (2015) argued that in RX J1713.7–3946, the efficient CR electron acceleration up to $\sim 10 \text{ TeV}$ currently at work has a tight physical connection with the ambient ISM. The authors showed that the distribution of the photon index Γ of the non-thermal X-rays, synchrotron X-rays, and both the gas-rich and -poor regions is small, with $\Gamma < 2.4$, and suggested that these regions correspond to the sites of high roll-off energy of the synchrotron emission. If the syn-

TABLE 4
RESULTS OF THE PROJECTED PROFILE TOWARDS THE NON-THERMAL X-RAY PEAKS

Name	Non-Thermal X-rays			$\langle N_p(H_2+H_I) \rangle$ ($\times 10^{21} \text{ cm}^{-2}$)	Separation Radio Peak (arcsec)
	l (deg)	b (deg)	Peak Intensity ($\times 10^{-5} \text{ counts s}^{-1} \text{ pixel}^{-1}$)		
(1)	(2)	(3)	(4)	(5)	(6)
NTX-N1	315.53	-2.08	2.56 ± 0.11	0.95 ± 0.04	-16
NTX-N2	315.56	-2.02	2.45 ± 0.06		-32
NTX-N3	315.34	-2.01	1.22 ± 0.05	0.96 ± 0.03	-48
NTX-N4	315.37	-1.96	0.401 ± 0.009		-48
NTX-NE1	315.72	-2.25	9.4 ± 0.2	0.94 ± 0.07	-16
NTX-NE2	315.66	-2.41	2.06 ± 0.10	3.6 ± 1.6	+64
NTX-NE3	315.70	-2.42	0.52 ± 0.02		+48
NTX-SW1	315.12	-2.38	8.8 ± 0.7	3.00 ± 0.15	+96
NTX-SW2	315.05	-2.44	0.490 ± 0.008		-16
NTX-SW3	315.17	-2.45	13.0 ± 0.5	3.04 ± 0.06	+32
NTX-SW4	315.25	-2.56	16.6 ± 1.2	3.19 ± 0.09	+16
NTX-SW5	315.40	-2.51	3.92 ± 0.09	2.45 ± 0.16	+240

NOTE. — Col. (1): X-ray peak name. Cols. (2–4): Physical properties of the non-thermal X-rays. Cols. (2–3): Position of the X-ray peak. Col. (4): Peak intensity of the X-ray. Col. (5): Mean proton column density $\langle N_p(H_2+H_I) \rangle$ within each region shown by Figure 9. Col. (6): Separation between each intensity peak of the X-ray and radio continua.

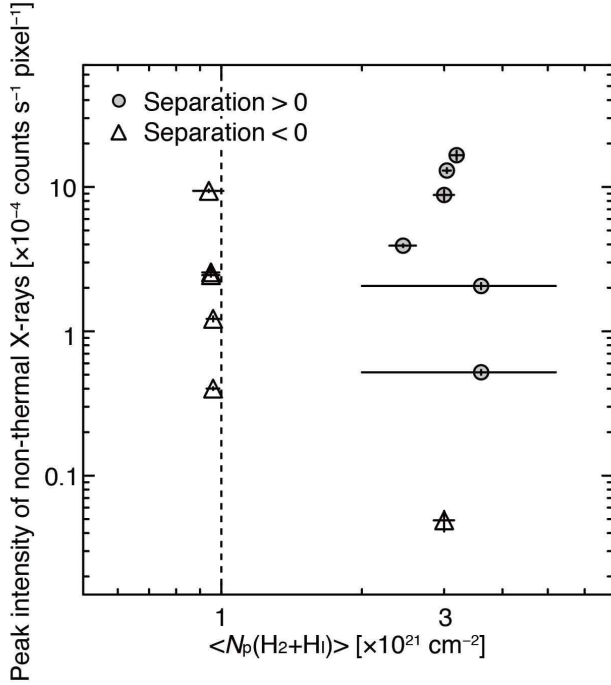


FIG. 11.— Correlation plot between the averaged proton column density $\langle N_p(H_2+H_I) \rangle$, and the peak intensity of non-thermal X-rays. Positive and negative separations (see text) are represented by circles and triangles, respectively, where the separation is defined as the distance between the non-thermal X-rays and radio continuum intensity peaks. The vertical dashed line indicates $\langle N_p(H_2+H_I) \rangle = 1 \times 10^{21} \text{ cm}^{-2}$.

chrotron cooling is efficient, the roll-off energy ε_0 of the synchrotron photons is given by the following equation (Zirakashvili & Aharonian 2007):

$$\varepsilon_0 = 0.55 \times (v_{\text{sh}} / 3000 \text{ km s}^{-1})^2 \eta^{-1} \text{ (keV)}, \quad (6)$$

where v_{sh} is the shock velocity, and $\eta = B^2 / \delta B^2$ (> 1) the degree of magnetic field fluctuations (the gyrofactor). The case of $\eta = 1$ is called the Bohm diffusion

limit and indicates the limit of the maximum magnetic turbulence. In the gas-rich/clumpy site, the shock-cloud interaction amplifies the turbulent magnetic field around dense gas clumps and the synchrotron X-rays are enhanced (e.g., Inoue et al. 2012). As a consequence, $\eta \sim 1$, hence increasing ε_0 . On the other hand, in the gas-poor/diffuse sites the shock waves are not decelerated, and the high v_{sh} results also in this case in a high ε_0 and, accordingly, in an enhancement in the X-rays emission. Sano et al. argued that the ambient conditions of the neutral ISM play a role in increasing the roll-off energy in the CR acceleration and the non-thermal X-rays. In what follows, we discuss the properties of the non-thermal X-rays in RCW 86 by comparing the X-ray properties in RX J1713.7–3946. The most intense non-thermal X-ray filaments in RCW 86 (Figure 1) are seen at the NE and SW. The average proton column density $\langle N_p(H_2 + H_I) \rangle$ is $0.94 \pm 0.07 \times 10^{21} \text{ cm}^{-2}$ in NTX-NE1 and $3.19 \pm 0.09 \times 10^{21} \text{ cm}^{-2}$ in NTX-SW4, i.e., they differ by a factor of three. In RCW 86 the gas-rich/clumpy region corresponds to the SW, and the gas-poor/diffuse region, to the NE. At the SW, however, the H I cloud does not have a CO clumpy counterpart. Unlike RX J1713.7–3946, there were no cold H I clumps detected as self-absorption features. Figure 13 shows the X-rays and the H I clump in SW. We see the thermal/non-thermal X-rays are enhanced around the cold H I clump. This suggests that shock-cloud interaction with the cold H I clump amplifies turbulence and magnetic field, causing the rim-brightened non-thermal X-rays. A similar enhancement of the thermal X-rays is seen. This indicates that the shock waves are heating up the surface of the cold H I clump. The H I peak brightness temperature of the clump is low, $\sim 58 \text{ K}$, suggesting that the clump has density $\sim 150 \text{ cm}^{-3}$ (Fukui et al. 2014, 2015). The same complementary spatial distribution between cold H I and X-rays due to shock-cloud interaction is also observed in RX J1713.7–3946 (see Figure 4 of Sano et al. 2013). It is also expected that the synchrotron X-ray flux will vary within a scale of several years due to the strong magnetic field (e.g., Uchiyama et al. 2007).

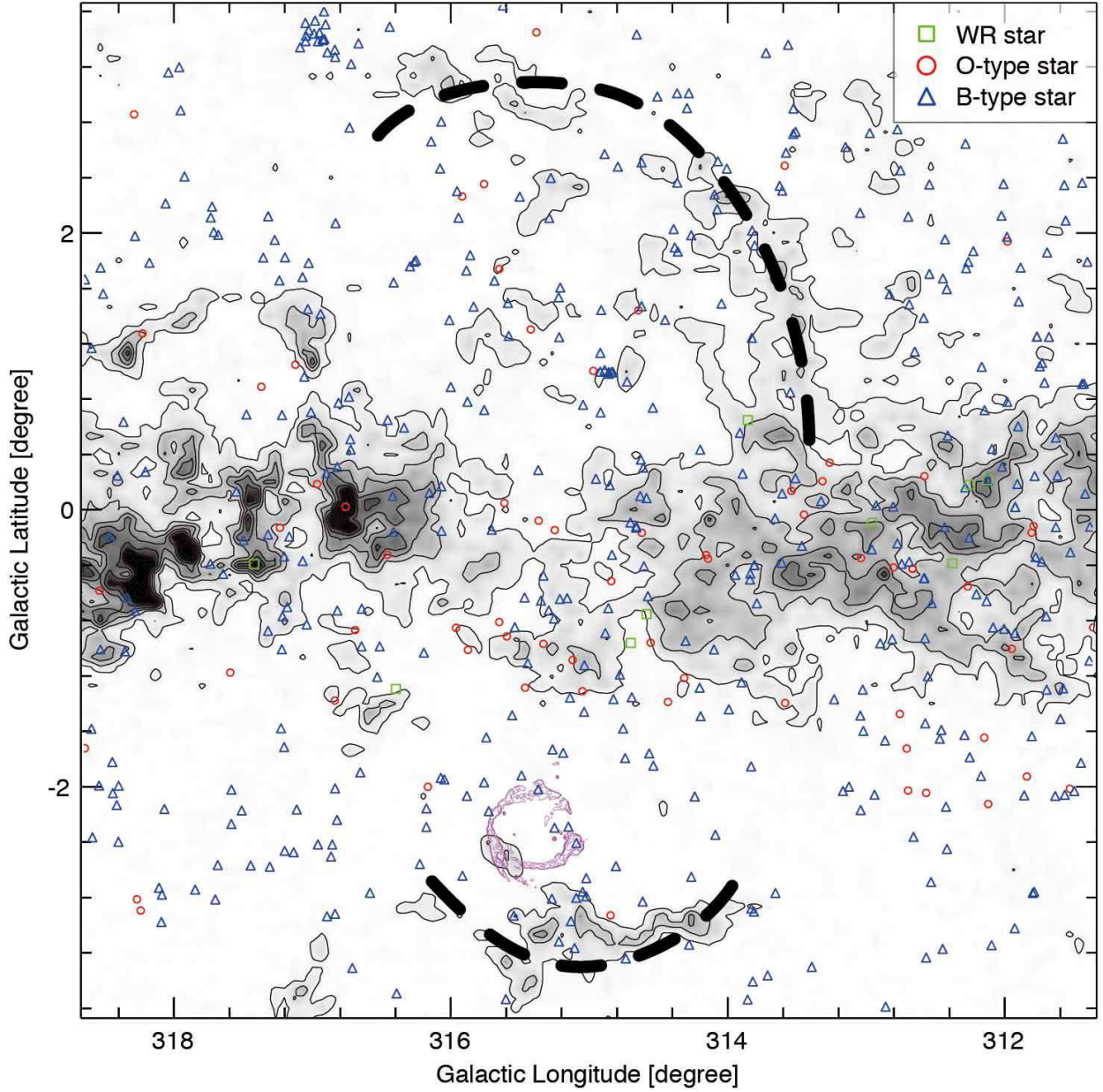


FIG. 12.— Large-scale integrated intensity map of the $^{12}\text{CO}(J=1-0)$ toward the RCW 86 taken with NANTEN (Matsunaga et al. 2001). The velocity range is from -40 to -30 km s^{-1} . The lowest contour level and contour interval of CO are 10 K km s^{-1} and 4 K km s^{-1} , respectively. Magenta contours indicate the MOST radio continuum at a frequency of 843 MHz as shown in Figure 1. The dashed lines represent the boundary of the CO supershell identified by Matsunaga et al. (2001).

Within the gas-poor/diffuse region at the NE, the acceleration by the fast shock is highly efficient. Figure 9 also shows that the ISM density at the NE is lower than at the SW and the N, as shown by the lower HI intensity. $\text{H}\alpha$ and X-ray observations indicate that the maximum shock velocity at the NE is $\sim 3,000$ km s^{-1} (with an average of $\sim 1,200$ km s^{-1}), 3–6 times larger than that at the SW and NW (Long & Blair 1990; Ghavamian et al. 2001; Helder et al. 2013). The difference in velocity by a factor of 3 corresponds to an ε_0 larger by an order of magnitude. We thus suggest that in the NE, the fast shock waves increased ε_0 and the intensity of the synchrotron radiation. It is suggested that the shock veloc-

ity at the SW has been slowing down rapidly for the last 200 years (Helder et al. 2013). This is consistent with the deformation of the shock front toward NTX-NE1 along the curved HI cavity-wall (see Northeast in Figure 9). In spite of that, the shock velocity remains three times higher than in the SW, suggesting that the HI gas is physically associated with the SNR. In 1,000 years we would expect that the shock waves in the NE will come into contact completely with the HI cavity wall and the X-rays will be enhanced by the shock-cloud interaction.

4.3. Forward and Reverse Shocks

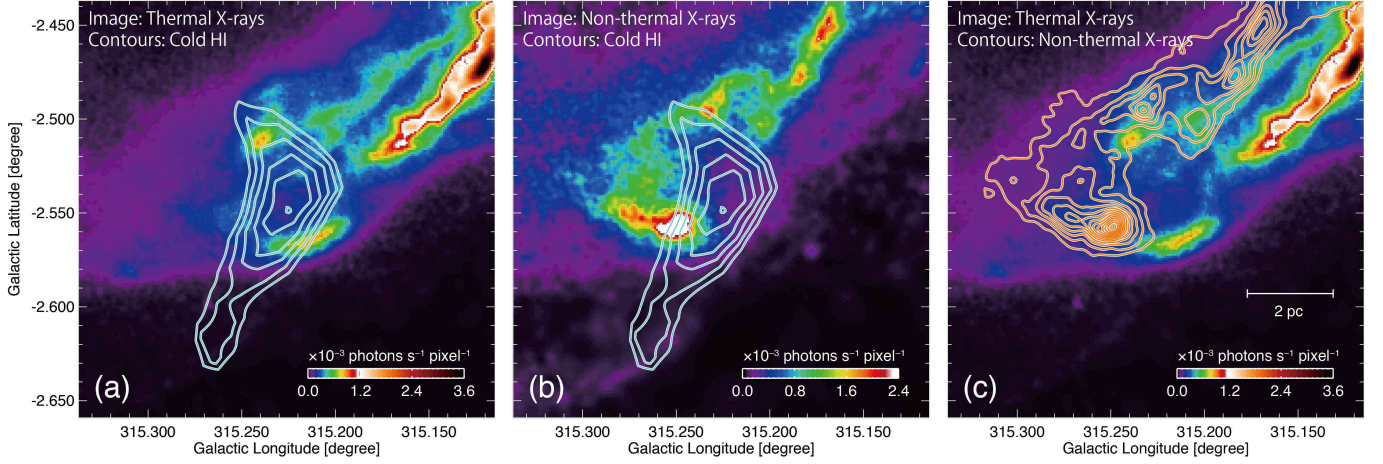


FIG. 13.— (a) Thermal X-ray image of RCW 86 in the energy range from 0.5 to 1.0 keV superposed with H I intensity contours (light blue) toward the southwest of the SNR. The color scale is linear, in units of 10^3 photons s^{-1} pixel $^{-1}$. The H I velocity is $V_{\text{LSR}} = -35$ km s^{-1} . The lowest contour level and contour interval of H I are 54 K ($\sim 72\sigma$) and 0.75 K ($\sim 1\sigma$), respectively. (b) Non-thermal X-ray image in the energy range from 2.0 to 4.5 keV, superposed with H I intensity contours. The color scale, unit, and contour levels are the same as in the left panel. (c) The same thermal X-ray image as Figure 13a, superposed with the non-thermal X-ray contours (orange). The lowest contour level and contour interval of the non-thermal X-rays are 5×10^{-5} photons s^{-1} pixel $^{-1}$ and 2.5×10^{-5} photons s^{-1} pixel $^{-1}$, respectively.

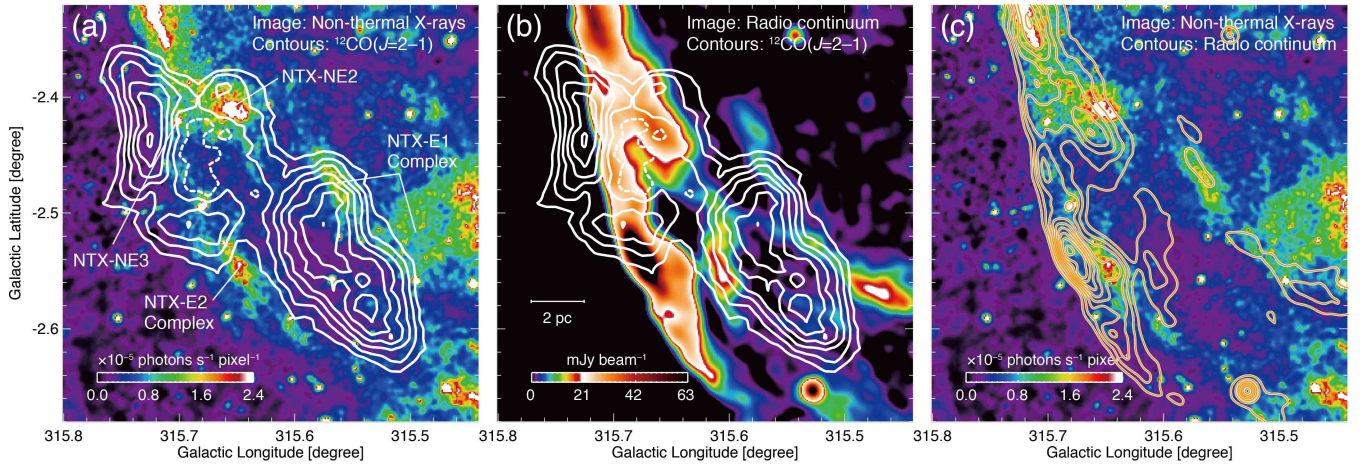


FIG. 14.— (a) Non-thermal X-ray image of RCW 86 in the energy range from 2.0 to 4.5 keV superposed with $^{12}\text{CO}(J=2-1)$ intensity contours (white) toward the east of the SNR. The color scale is linear, and is given in units of 10^5 photons s^{-1} pixel $^{-1}$. The CO velocity range is the same as Figure 6 East. The lowest contour level and the contour interval of CO are 2.1 K ($\sim 15\sigma$) and 1.0 K ($\sim 10\sigma$), respectively. (b) Radio continuum image superposed on $^{12}\text{CO}(J=2-1)$ intensity contours (white). The linear color scale is given in mJy beam $^{-1}$. The contour levels are the same as in the left panel. (c) Same non-thermal X-ray image as in Figure 14a, superposed with radio continuum contours (orange). The lowest contour level and the contour interval of the radio continuum are 7 mJy beam $^{-1}$ and 10 mJy beam $^{-1}$, respectively.

In this section we discuss the forward and reverse shocks in RCW 86. Based on *Chandra* observations toward the SW shell, Rho et al. (2002) showed that relativistic CR electrons are accelerated by the reverse shock, since the non-thermal X-rays are located at the interior of the heated H I traced by thermal X-rays. In addition, the different spatial distributions of radio continuum emission and non-thermal X-rays reflect the different energy ranges of the emitting CR electrons. For a magnetic field of $10 \mu\text{G}$, the synchrotron radiation whose peak is $h\nu = 4$ keV loses the energy at a decay timescale of only 900 years, while the CR electrons emitting at 1 GHz radio continuum can radiate over 10^7 years. The synchrotron

X-rays originate in the high-energy electrons close to the shock front and the radio emission from lower energy electrons downstream (Rho et al. 2002). Ueno et al. (2007) and Yamaguchi et al. (2011) studied the Fe ejecta distribution over the SNR and showed that highly ionized Fe ejecta are likely heated up by the reverse shock.

Our comparative study of multi-wavelength observations of the ISM provides a tool to discriminate the reverse shock and the forward shock in different regions. In Figure 11 we showed the relative location between the non-thermal X-ray peaks and radio peaks in the radial distribution. The positive values of the separation (Separation > 0) correspond to the case in which the

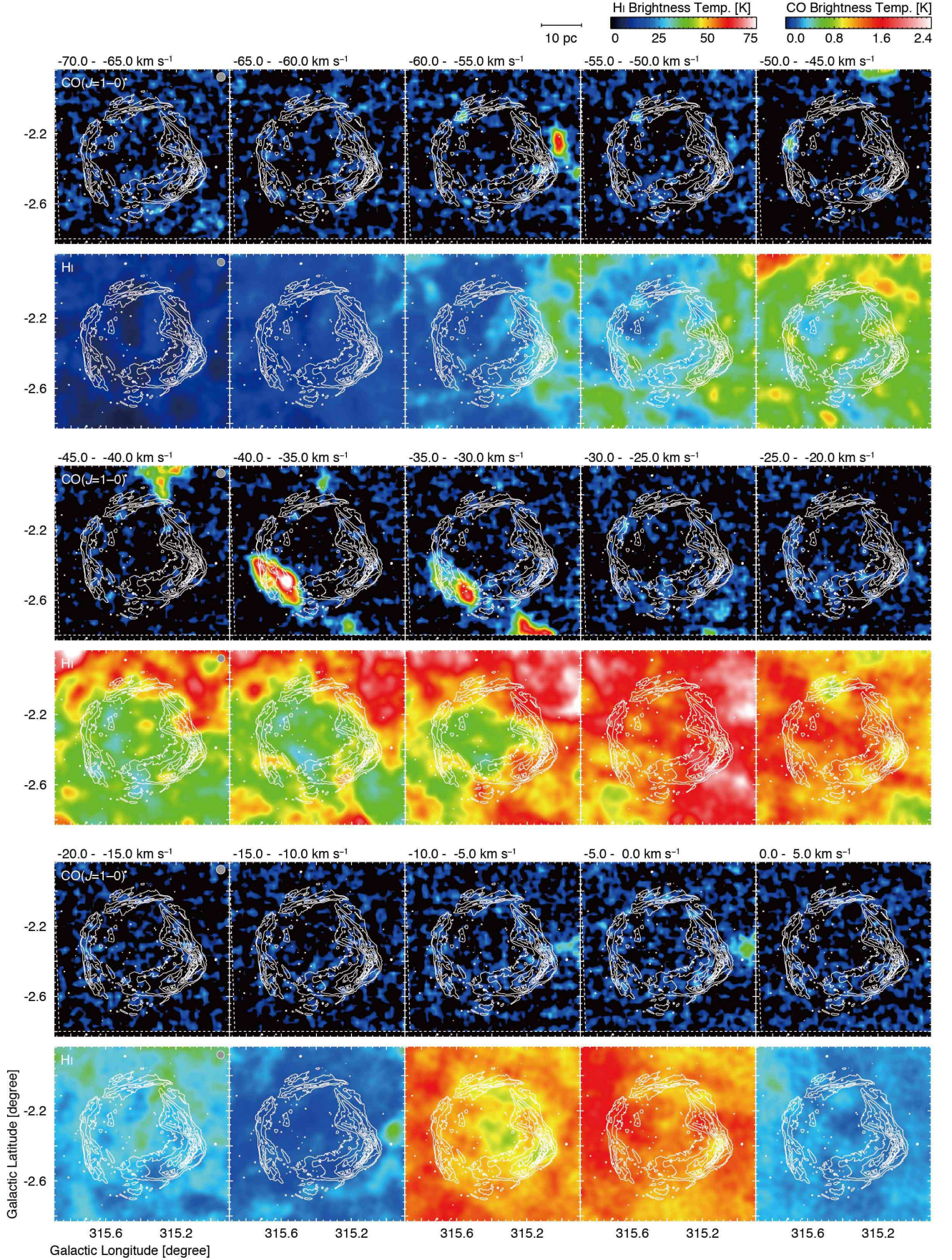


FIG. A.1.— Velocity channel distributions of the $^{12}\text{CO}(J=1-0)$ and HI brightness temperatures superposed with the same X-ray intensity contours as in Figure 3a. Each panel of CO/HI shows intensity distributions averaged every 5 km s^{-1} in a velocity range from -70 to $+5 \text{ km s}^{-1}$. The scale and color bars for HI and CO are shown on top of the set of panels.

non-thermal X-ray peaks are located farther inside than the nearest radio peak, while the negative values of the separation (Separation < 0) correspond to the opposite case. Rho et al. (2002) interpreted that the former case corresponds to the reverse shock and the latter, to the forward shock.

The reverse shock is located only in regions with the average gas column density $\langle N_p(\text{H}_2 + \text{HI}) \rangle > 10^{21} \text{ cm}^{-2}$, whereas the forward shock is located, except for one point, in regions with the average gas column density $\langle N_p(\text{H}_2 + \text{HI}) \rangle < 10^{21} \text{ cm}^{-2}$. This supports the idea that the reverse shock recoiled after collision with the ISM. It is possible that the exceptional point be explained if the shock slipped through the clumpy gas-rich region. Conversely, in the gas-poor region the reverse shock has not been detected. Particularly, toward the dense clumpy CO -37 E the forward/reverse shock has a complicated distribution. Figure 14 shows the X-ray non-thermal and radio continuum distribution of CO -37 E. The upper right corner of the images points in the direction of the SNR center. In addition to the NTX-NE2-3 complexes, we find various non-thermal X-ray filaments similar to NTX-E1-2 as a representative case and the filaments show complimentary distributions to the clumpy CO clouds. We see a trend consisting in the non-thermal X-rays being located more in the inner part than the radio continuum. In the typical region NTX-NE2-3, the separation between the non-thermal and radio continuum is 48–64 arcsec, which is equivalent to 0.6–0.8 pc at 2.5 kpc. The shock speed of this area is estimated to be $1,653 \pm 228 \text{ km s}^{-1}$ by Helder et al. (2013). If we assume that the reverse shock and the forward shock are moving at the same velocity, the shock wave collided with the molecular cloud 400 yrs ago. This agrees well with the shock age < 380 yr of Fe ejecta (e.g., Yamaguchi et al. 2008).

In addition, the reverse shock may hold the key to understand an efficient acceleration mechanism of CR electrons with $\sim 1 \text{ TeV}$ or higher. According to the numerical simulations, turbulence in downstream regions can create strong magnetic fields, up to mG or $\sim 50 \mu\text{G}$ on average (e.g., Inoue et al. 2012). In this unusual situation, some additional acceleration mechanisms will become important, including acceleration with magnetic reconnection (e.g., Hoshino 2012), reverse shock acceleration (e.g., Ellison 2001), non-linear effect of DSA (e.g., Malkov & Drury 2001), second-order Fermi acceleration (Fermi 1949), etcetera. Detailed X-ray spectroscopy and comparative studies with the interstellar gas will reveal efficient acceleration mechanisms of CR electrons.

To summarize, a thorough investigation of the ISM is extremely important to study the progenitor system, the origin of thermal X-rays, the acceleration mechanism of CR electrons, and the shock dynamics of SNRs. Observations of the ISM at high angular resolution better than 45 arcsec will allow us to make a comparison of small-scale structures of the ISM with observations at the other wavelengths, and will enable us to pursue more detailed physical process. A spectral analysis of the X-ray data is indispensable to derive the distributions of the photon index and the roll-off energy and provide a firm basis to elucidate the relationship between the CR acceleration and the ISM. The synchrotron radiation above 10 keV from the electrons accelerated by the reverse shock will be ob-

tained in the hard X-ray imaging with *Nustar*. *Chandra* high-resolution measurements of the proper motion will reveal the kinematics of the X-ray filaments in detail.

5. CONCLUSIONS

We summarize the present work as follows.

1. We have revealed atomic and molecular gas associated with the young TeV γ -ray SNR RCW 86 by using NANTEN2 CO and ATCA & Parkes HI datasets. The HI gas is distributed surrounding the X-ray shell and shows a cavity-like distribution with an expanding velocity of $\sim 7 \text{ km s}^{-1}$, while the CO clouds are located only in the east, south, and northwest, showing the high-intensity ratio of CO $J = 2-1/1-0$ ratio > 0.8 enhanced by the shock heating and/or compression in the surface of the clouds.
2. Thermal X-ray filaments show a good spatial correspondence with the HI wall and small-scale structures of CO clouds. We also found a correlation between the total proton column density and the thermal X-ray intensity. This indicates that the atomic/molecular gas of density $10-100 \text{ cm}^{-3}$ is associated with the SNR shockwaves.
3. Non-thermal X-rays are bright both in the gas-rich and -poor regions. We interpret that the shock-cloud interaction between the cold HI clumps and the high shock velocity could enhance the non-thermal X-rays, which is a situation similar to that discussed by Sano et al. (2015) in the SNR RX J1713.7–3946. In addition, the reverse shock is detected only in the gas-rich region with a total proton column density of $\sim 10^{21} \text{ cm}^{-2}$ or higher.
4. Our study confirms that the progenitor of RCW 86 was a system consisting of a white dwarf and a low-mass star with low-velocity accretion winds, as suggested by Williams et al. (2011).

ACKNOWLEDGEMENTS

We are grateful to Aya Bamba, Takaaki Tanaka, Hiroyuki Uchida, and Hiroya Yamaguchi for thoughtful comments and their contribution on the X-ray properties. We acknowledge Anne Green for her valuable support during the HI observations and reduction, and Gloria M. Dubner, PI of the ATCA project C1011 carried out to obtain the reported HI data, who provided them to Yasuo Fukui. We also acknowledge to Shinya Tabata, Momo Hattori, Shigeki Shimizu, Sho Soga, Daichi Nakashima, Shingo Otani, Yutaka Kuroda, Masashi Wada, Ryo Kaji, Keisuke Hasegawa, and Rey Enokiya for contributions on the observations of $^{12}\text{CO}(J = 1-0)$ data. This work was financially supported by Grants-in-Aid for Scientific Research (KAKENHI) of the Japanese society for the Promotion of Science (JSPS, grant Nos. 22740119, 12J10082, 24224005, 15H05694, and 16K17664). This work also was supported by “Building of Consortia for the Development of Human Resources in Science and Technology” of Ministry of Education, Culture, Sports, Science and Technology (MEXT, grant No. 01-M1-0305). This research was based on observations obtained

with *XMM-Newton*, an ESA science mission with instruments and contributions directly funded by ESA Member States and NASA. We also utilize data from MOST and SHASSA. The Molonglo Observatory Synthesis Telescope (MOST) is operated by The University of Sydney with support from the Australian Research Council and the Science Foundation for Physics within The University of Sydney. The Southern H-Alpha Sky Survey Atlas (SHASSA) is supported by the National Science Foundation. EMR is member of the Carrera del Investigador Científico of CONICET, Argentina, and is partially supported by CONICET grant PIP 112-201207-00226.

APPENDIX: VELOCITY CHANNEL MAPS OF CO AND HI

Figure A.1 shows the velocity channel distributions of the $^{12}\text{CO}(J=1-0)$ and HI brightness temperature every

5 km s $^{-1}$ from -70 km s $^{-1}$ to $+5$ km s $^{-1}$ superposed with the X-ray intensity contours. First, we investigated the spatial correlation and anti-correlation between the X-ray and interstellar gas (CO and HI) distributions. We found that the X-ray shell is complementary to the CO/HI structure at a radial velocity of ~ -35 km s $^{-1}$. In particular, the HI cavity and its expanding motion showed evidence for the association with the SNR shocks (see also Figure 5 and Section 3.3). Ajello et al. (2016) presented the image of the HI cavity-like structure, but the authors did not mention the existence of an expanding shell motion. Apparently, the HI cloud at a radial velocity from -10 to 0 km s $^{-1}$ is also well correlated with the X-ray shell; however, as it is a local cloud component, we ignored it from the standpoint of interaction with the SNR.

REFERENCES

- Aharonian, F., Akhperjanian, A. G., Bazer-Bachi, A. R., et al. 2008, *A&A*, 481, 401
- Aharonian, F., Akhperjanian, A. G., de Almeida, U. B., et al. 2009, *ApJ*, 692, 1500
- Ajello, M., Baldini, L., Barbiellini, G., et al. 2016, *ApJ*, 819, 98
- Badenes, C., Hughes, J. P., Bravo, E., & Langer, N. 2007, *ApJ*, 662, 472
- Bamba, A., Koyama, K., & Tomida, H. 2000, *PASJ*, 52, 1157
- Bell, A. R. 1978, *MNRAS*, 182, 147
- Bertsch, D. L., Dame, T. M., Fichtel, C. E., et al. 1993, *ApJ*, 416, 587
- Blandford, R. D., & Ostriker, J. P. 1978, *ApJ*, 221, L29
- Brand, J., & Blitz, L. 1993, *A&A*, 275, 67
- Broersen, S., Chiotellis, A., Vink, J., & Bamba, A. 2014, *MNRAS*, 441, 3040
- Cassam-Chenaï, G., Decourchelle, A., Ballet, J., et al. 2004, *A&A*, 427, 199
- Chevalier, R. A., Kirshner, R. P., & Raymond, J. C. 1980, *ApJ*, 235, 186
- Claas, J. J., Kaastra, J. S., Smith, A., Peacock, A., & de Korte, P. A. J. 1989, *ApJ*, 337, 399
- Clark, D. H., & Stephenson, F. R. 1975, *The Observatory*, 95, 190
- Dickey, J. M., & Lockman, F. J. 1990, *ARA&A*, 28, 215
- Duvidovich, L., Dubner, G., Giacani E., et al. 2016, *BAAA*, 58, 212
- Ellison, D. C. 2001, *Space Sci. Rev.*, 99, 305
- Fermi, E. 1949, *Physical Review*, 75, 1169
- Fukuda, T., Yoshiike, S., Sano, H., et al. 2014, *ApJ*, 788, 94
- Fukui, Y., Moriguchi, Y., Tamura, K., et al. 2003, *PASJ*, 55, L61
- Fukui, Y., Sano, H., Sato, J., et al. 2012, *ApJ*, 746, 82
- Fukui, Y., Okamoto, R., Kaji, R., et al. 2014, *ApJ*, 796, 59
- Fukui, Y., Torii, K., Onishi, T., et al. 2015, *ApJ*, 798, 6
- Gaustad, J. E., McCullough, P. R., Rosing, W., & Van Buren, D. 2001, *PASP*, 113, 1326
- Ghavamian, P., Raymond, J., Smith, R. C., & Hartigan, P. 2001, *ApJ*, 547, 995
- Hachisu, I., Kato, M., & Nomoto, K. 1996, *ApJ*, 470, L97
- Helder, E. A., Vink, J., Bamba, A., et al. 2013, *MNRAS*, 435, 910
- H. E. S. S. Collaboration, Abramowski, A., Aharonian, F., et al. 2016, *arXiv:1601.04461*
- Helou, G., & Walker, D. W. 1988, *Infrared astronomical satellite (IRAS) catalogs and atlases. Volume 7*, p.1-265, 7, 1
- Hill, E. R. 1967, *Australian Journal of Physics*, 20, 297
- Hoshino, M. 2012, *Physical Review Letters*, 108, 135003
- Inoue, T., Yamazaki, R., Inutsuka, S.-i., & Fukui, Y. 2012, *ApJ*, 744, 71
- Ishihara, D., Onaka, T., Kataza, H., et al. 2010, *A&A*, 514, A1
- Kaastra, J. S., Asaoka, I., Koyama, K., & Yamauchi, S. 1992, *A&A*, 264, 654
- Kaplan, D. L., Frail, D. A., Gaensler, B. M., et al. 2004, *ApJS*, 153, 269
- Kuntz, K. D., & Snowden, S. L. 2008, *A&A*, 478, 575
- Kesteven, M. J., & Caswell, J. L. 1987, *A&A*, 183, 118
- Kulesa, C. A., Hungerford, A. L., Walker, C. K., Zhang, X., & Lane, A. P. 2005, *ApJ*, 625, 194
- Lemoine-Goumard, M., Renaud, M., Vink, J., et al. 2012, *A&A*, 545, A28
- Long, K. S., & Blair, W. P. 1990, *ApJ*, 358, L13
- Malkov, M. A., & Drury, L. O. 2001, *Reports on Progress in Physics*, 64, 429
- Matsunaga, K., Mizuno, N., Moriguchi, Y., et al. 2001, *PASJ*, 53, 1003
- Maxted, N. I., Rowell, G. P., Dawson, B. R., et al. 2013, *PASA*, 30, e055
- Moriguchi, Y., Tamura, K., Tawara, Y., et al. 2005, *ApJ*, 631, 947
- Mills, B. Y., Slee, O. B., & Hill, E. R. 1961, *Australian Journal of Physics*, 14, 497
- Nomoto, K., Saio, H., Kato, M., & Hachisu, I. 2007, *ApJ*, 663, 1269
- Rho, J., Dyer, K. K., Borkowski, K. J., & Reynolds, S. P. 2002, *ApJ*, 581, 1116
- Ridge, N. A., Di Francesco, J., Kirk, H., et al. 2006, *AJ*, 131, 2921
- Rosado, M., Ambrocio-Cruz, P., Le Coarer, E., & Marcelin, M. 1996, *A&A*, 315, 243
- Ruiz, M. T. 1981, *ApJ*, 243, 814
- Sakamoto, S., Hasegawa, T., Handa, T., Hayashi, M., & Oka, T. 1997, *ApJ*, 486, 276
- Sano, H., Sato, J., Horachi, H., et al. 2010, *ApJ*, 724, 59
- Sano, H., Tanaka, T., Torii, K., et al. 2013, *ApJ*, 778, 59
- Sano, H., Fukuda, T., Yoshiike, S., et al. 2015, *ApJ*, 799, 175
- Sault, R. J., Teuben, P. J., & Wright, M. C. H. 1995, *Astronomical Data Analysis Software and Systems IV*, 77, 433
- Seta, M., Hasegawa, T., Dame, T. M., et al. 1998, *ApJ*, 505, 286
- Smith, R. C. 1997, *AJ*, 114, 2664
- Strüder, L., Briel, U., Dennerl, K., et al. 2001, *A&A*, 365, L18
- Takahashi, T., Tanaka, T., Uchiyama, Y., et al. 2008, *PASJ*, 60, S131
- Turner, M. J. L., Abbey, A., Arnaud, M., et al. 2001, *A&A*, 365, L27
- Uchiyama, Y., Aharonian, F. A., Tanaka, T., Takahashi, T., & Maeda, Y. 2007, *Nature*, 449, 576
- Ueno, M., Sato, R., Kataoka, J., et al. 2007, *PASJ*, 59, 171
- Vink, J., Kaastra, J. S., & Bleeker, J. A. M. 1997, *A&A*, 328, 628
- Westerlund, B. E. 1969, *AJ*, 74, 879
- Whiteoak, J. B. Z., & Green, A. J. 1996, *A&AS*, 118, 329
- Williams, B. J., Blair, W. P., Blondin, J. M., et al. 2011, *ApJ*, 741, 96
- Yamaguchi, H., Koyama, K., Nakajima, H., et al. 2008, *PASJ*, 60, S123
- Yamaguchi, H., Koyama, K., & Uchida, H. 2011, *PASJ*, 63, S837
- Yamaguchi, H., Katsuda, S., Castro, D., et al. 2016, *ApJ*, 820, L3
- Yoshiike, S., Fukuda, T., Sano, H., et al. 2013, *ApJ*, 768, 179
- Yuan, Q., Huang, X., Liu, S., & Zhang, B. 2014, *ApJ*, 785, L22
- Zhao, F.-Y., Strom, R. G., & Jiang, S.-Y. 2006, *ChJAA*, 6, 635
- Zirakashvili, V. N., & Aharonian, F. 2007, *A&A*, 465, 695